ABSTRACT

Title of dissertation: NONLINEARITY BASED
ACOUSTIC WAVE REDIRECTION

Saliou B. Telly
Doctor of Philosophy, 2018

Dissertation directed by: Professor Balakumar Balachandran
Mechanical Engineering

Advances in metamaterials technology have revealed novel opportunities for achieving peculiar material properties amenable to the control of wave propagation paths for various applications not realizable with conventional materials. Some prominent examples are schemes for electromagnetic and acoustic cloaking and focusing devices. In the classical approach to the formulations of these devices, one exploits a change of physical coordinates to achieve a desired wave behavior within a finite space. Such a change can be interpreted as a transformation of material properties when the field equations of interest are invariant to coordinate transformations. To date, this intuitive approach has led to the formulation of various two-dimensional devices for wave redirection, including infinite circular and square cloaks for both electromagnetic and acoustic fields. For acoustic fields, however, the transformation approach is constrained to fluid-like metamaterials amenable to the propagation of longitudinal waves only. Complications arise with solid materials because of their inherent ability to sustain the propagation of both longitudinal

and transverse waves, which refract differently in linear materials due to dissimilar propagation speeds.

In this dissertation, the author first seeks a sequence of transformations that may be used for cloaking two-dimensional airfoil sections through the classical transformation method. For the sought sequence, the author takes advantage of the mapping properties of the Joukowsky Transformation, and the closely related Kaman-Trefftz Transformation, which are two well-known complex mappings that have classically been used in the study of the aerodynamics of airfoil sections. Next, the author explores wave redirection mechanisms that may take advantage of nonlinear wave phenomena in elastic solid materials for acoustic wave redirection. Starting from the classical nonlinear Murnaghan model, a hyper-elastic material is formulated to realize couplings between shear and compressional modes that could lead to a more suitable refractive behavior for acoustic wave redirection in a solid metamaterial. The formulated model is studied by using perturbation and approximation techniques.

The findings of this dissertation can be useful for redirecting and manipulating acoustic waves for practical applications.

NONLINEARITY BASED ACOUSTIC WAVE REDIRECTION

by

Saliou B. Telly

Dissertation submitted to the Faculty of the Graduate School of the
University of Maryland, College Park in partial fulfillment
of the requirements for the degree of
Doctor of Philosophy
2018

Advisory Committee:
Professor Balakumar Balachandran, Mechanical Engineering, Chair and Advisor
Professor Amr Baz, Mechanical Engineering
Professor Teng Li, Mechanical Engineering
Professor Miao Yu, Mechanical Engineering
Professor Sung Lee, Aerospace Engineering, Dean's Representative

Dedication

To my wife and my two daughters
for their love, patience, and support

Acknowledgments

First, I would like to thank my dissertation committee. I am particularly thankful to my advisor, Professor Balakumar Balachandran for his guidance, patience, and encouragement throughout the completion of this dissertation thesis. I am most grateful for his technical knowledge, and his ability to push beyond what I often thought to be the frontiers of my aptitudes.

Further, I would like to express my appreciation to my former and current labmates, for their contribution to the successful completion of this dissertation through their friendship, support, and rich academic discussions.

I am forever indebted to American University for supporting and facilitating my pursue of an engineering education at the University of Maryland while I was a student athlete on scholarship at American University. This atypical accommodation was at the origin of my long educational journey in engineering that is culminated by the completion of the dissertation.

I am also thankful to the US Navy, and particularly to the Naval Surface Warfare Center, Carderock Division, for the educational and research opportunities that it offered, which allowed me to further my graduate education and conduct basic science research that supported this dissertation.

Last, I would like to thank my family and many friends for their patience and support throughout this journey. I am particularly thankful to my wife for being the backbone of my support structure through nearly two decades of academic endeavor to the completion of this dissertation.

Table of Contents

List of Figures

Chapter 1: Introduction

1.1 Background

The bending phenomenon of waves as they propagate through media of different refractive properties has long been exploited for practical applications in various wave fields. In the optical field, for instance, devices such as microscopes and telescopes that use engineered refractive lenses for magnification and focusing, have been around for several centuries now [1]. While less trivial applications were found in fields such as underwater acoustics where submariners have known for many decades to exploit convergence and shadow zones created by the natural refractive characteristics of the ocean for tactical purposes [2]. Thus, it is needless to persuade that refraction has been extensively investigated to date for controlling wave propagation paths. However, recent advances in metamaterials technology have led to renewed interest in the phenomenon. Metamaterials are artificially designed materials that exhibit peculiar wave interaction properties seldom found in natural or conventionally engineered material [3]. The field stemmed from the counter-intuitive property of negative index of refraction (NIR), which can be traced back to the vision of the Russian physicist Victor Veselago in 1967 [4]. Veselago postulated then that although all known natural and engineered materials at the time had a positive in-

dex of refraction, nothing precluded in theory from having NIR materials and that such property was achievable if both the electrical permitivity ϵ and the magnetic permeability μ of a material were allowed to be negative; that is, $\epsilon < 0, \mu < 0$ [4]. As a potential application, Veselago demonstrated that a flat lens could be designed with NIR materials [4]. Despite their scientific merit and implications, NIR materials proposed by Veselago remained a mere academic curiosity for more than three decades as no known material had the required negative permeability ($\mu < 0$) [5]. However, in 2000, with advances in material fabrication techniques, a group of scientists, Smith *et al.*, successfully designed and demonstrated the first NIR material at the University of California in San Diego [6]. To achieve the required negative permitivity ($\epsilon < 0$) and permeability ($\mu < 0$) postulated by Veselago, Smith's group used an array of split ring resonators and metal posts, designed at the sub-wavelength scale [4]. Their work was groundbreaking, and several efforts were soon underway to explore potential applications of NIRs and metamaterials technology. A noteworthy effort, among others, was the work of the British scientist John Pendry, who demonstrated that a "perfect lens" can be designed to achieve imaging beyond Abbe's diffraction limit by using NIR materials [7]. Thought this was momentous in itself, particularly for focusing devices in the optical field, it is rather Pendry's introduction of a transformation-based approach to formulating wave redirection devices [8] a few years later that has arguably been the most consequential and thrusting discovery to date for metamaterials research. In a seminal paper published in 2006, Pendry presented a systematic means to formulating devices for electromagnetic

wave redirection [8]. Starting from the known invariance of Maxwell's equations under coordinate transformations, Pendry demonstrated that a geometric transformation of a virtual electromagnetic domain with permitivity ϵ, and permeability μ, can simply be interpreted as a real physical domain with new properties ϵ' and μ', which relate to those of the virtual domain through simple formulae involving the gradient of the deformation [8]. As an immediate consequence of his findings, Pendry formulated in the same paper the properties of a three-dimensional cloaking device capable of rendering an enclosed object invisible to an electromagnetic wave field [8]. Shortly thereafter, a physical realization of a two-dimensional electromagnetic cloak based on Pendry's formulation was achieved by Smith *et al.* of Duke University using split ring resonators [9]. Pendry's work and the ensuing experimental demonstration were major milestones, and sparked various efforts to explore the possibility of extending the transformation approach to other classical waves fields, including elastodynamic waves. However, Milton demonstrated later in the same year that in the general case, the three-dimensional elastodynamic equations did not maintain the same invariance properties as Maxwell's equations under coordinate transformations; therefore, violating a fundamental premise of Pendry's transformation approach [10]. Nonetheless, Milton's work did not exclude the possibility for the special case of acoustic waves in fluid media where the necessary invariance of the equations to coordinates change remained valid [10]. In fact, to date, numerous acoustic wave redirection devices, including acoustic cloaks, lenses, beam shifters, and field rotators, have been formulated by using the transformation approach [5]. However, despite their successful formulation, the aforementioned refraction based

acoustic devices present major realization and practicability challenges due to the fluid-like properties inherent to their formulation. As a results, more than a decade since Pendry's first introduction of the transformation approach, the formulation of acoustic wave redirection materials and devices remains an active area of research.

1.2 Scope of Dissertation

In the present dissertation, the author explores the problem of bending and controlling acoustic waves by using materials with unusual properties. The specific objectives are to examine various approaches, including the use of geometric transformations and the modification of constitutive laws to formulate materials that can be used for the redirection of waves for practical applications. The scope of the dissertation is two-fold. First, a sequence of transformations is sought for cloaking airfoil geometries by using the transformation approach to wave redirection. The interest in airfoil geometries is their practical relevance to both electromagnetics and acoustics due to their use as control structures for vehicles operating in air and undersea. In the sought sequence of transformations, the author exploits Joukowsky and Karman-Trefftz maps, two complex variable transformations that have been instrumental in the earlier studies of the aerodynamic of airfoils. In a second facet of the investigation, the redirection of acoustic waves using elastic materials is explored. Exploiting nonlinearity and nonlinear wave phenomena, a hyper-elastic material favorable to controlling acoustic wave propagation paths is formulated. The formulation stems from modifications to the Murnaghan strain

energy function, a classical hyper-elastic material model, to help achieve a transfer of energy from the longitudinal wave propagation mode to the transverse mode through nonlinear couplings.

The dissertation is organized as follow. In this first introductory chapter, a brief review of pertinent literature is presented to provide context for this work. In Chapter 2, the Transformation Method is reviewed and its practicability for the formulation of acoustic devices is discussed. In Chapter 3, the author's effort to derive a sequence of transformations exploitable for cloaking two-dimensional airfoil geometries is summarized. In Chapter 4, the formulation of a hyper-elastic material amenable acoustic wave redirection is presented. Chapter 5 contains a discussion of the findings, conclusions reached from the dissertation work, and recommendations for future work.

Chapter 2: Transformation Approach to Wave Redirection

2.1 Overview

In the introductory chapter the author presented a brief background of the efforts to exploit advances in metamaterials technology to design wave redirection devices for practical applications. A particular mention was made of Pendry for his introduction of the transformation approach to wave redirection, which has been a groundbreaking contribution to the state of the art of metamaterial research. In the present chapter, the author presents in more details this intuitive and straightforward methodology for formulating the properties of wave redirection devices. The necessary mathematical foundations are first introduced, which is followed by a presentation of the methodology and its applications to the formulation of wave redirection devices in electromagnetics and acoustics. The author gives particular attention to the formulation of cloaking devices, which is pertinent to the first part of this dissertation work.

2.1.1 Mathematical Foundations

The fundamental premise of the transformation approach to formulate the material properties of devices for wave redirection is based on the invariance of the governing equations of the wave fields of interest to change of coordinates. To best understand how a transformation of physical coordinates can translate to material properties when the field equations are invariant to coordinate changes, one must revisit the transformation rules for vectors and tensors, which are invariant quantities under a change of basis [11]. These rules are often introduced as mathematical fundamentals in graduate courses in continuum mechanics or elasticity and can be found in many classical textbooks.

Before proceeding with the discussion, a brief summary on the notational conventions adopted throughout this dissertation is warranted. As in many classical textbooks, scalar quantities are represented by italic or greek letters, for example, a or α while vectors and tensors are represented by bold font letters, for example, $\mathbf{v}$ or $\mathbf{A}$. To some exceptions, lower-case bold font letters are mainly used for vectors while upper-case bold font letters are reserved for tensor quantities. Components of vector and tensor quantities are represented by italic letters with subscripts, for example, v_i or A_{ij}. Subscripts are also used to indicate partial differentiation when preceded by a comma as would be trivial from the context. The scalar and vector products of two vectors $\mathbf{u}$ and $\mathbf{v}$ are represented respectively by $\mathbf{u}\cdot\mathbf{v}$ and $\mathbf{u}\times\mathbf{v}$, and the tensor product is represented by $\mathbf{u}\otimes\mathbf{v}$. The second order tensor $\mathbf{u}\otimes\mathbf{v}$ is defined as $(\mathbf{u}\otimes\mathbf{v})\cdot\mathbf{w} = (\mathbf{v}\cdot\mathbf{w})\mathbf{u}$. Einstein summation convention over repeated indices is

also assumed, i.e, the appearance of an index twice in a term, implies a summation of that term over the range of the repeated index. Unless otherwise stated, the range of indices can be assumed to be $\{1, 2, 3\}$, for example, $u_i\mathbf{e_i} = u_1\mathbf{e_1} + u_2\mathbf{e_2} + u_3\mathbf{e_3}$. The conventional vector calculus notation is adopted for differential operators such the gradient, curl, divergence, and Laplacian.

Let a vector $\mathbf{u} = u_i\mathbf{e_i}$ in a Cartesian coordinate system with orthonormal basis vectors $\mathbf{e_i}$ be re-expressed as $\mathbf{u'} = u'_i\mathbf{e'_i}$ in a new Cartesian coordinate system with orthonormal basis vectors $\mathbf{e'_i}$. Since $\mathbf{u}$ and $\mathbf{u'}$ are the same vector that is simply expressed in two different coordinate systems, that is, $u'_i\mathbf{e'_i} = u_i\mathbf{e_i}$, the relationship between the components u'_i and u_i of $\mathbf{u}$ in the two Cartesian coordinate systems can be established and is given by Eq. (2.1).

$$u'_i = A_{ij}u_j \text{ or } \mathbf{u'} = \mathbf{Au} \tag{2.1}$$

Here, $A_{ij} \coloneqq e'_i \cdot e_j$ are the components of the tensor $\mathbf{A}$.

The transformation rules for vectors; that is, Eq. (2.1), can be extended to second order tensors by recalling that second order tensors relate two vector quantities. Thus, let two vectors $\mathbf{u}$ and $\mathbf{v}$ in a Cartesian coordinate system of orthonormal basis vectors $\mathbf{e_i}$ be related by the second order tensor $\mathbf{S}$ such that $\mathbf{v} = \mathbf{Su}$. The relationship between $\mathbf{u}$ and $\mathbf{v}$ can be expressed in component form as shown below in Eq. (2.2).

$$v_i\mathbf{e_i} = (S_{ij}\mathbf{e_i} \otimes \mathbf{e_j}) \cdot (u_k\mathbf{e_k}) = S_{ij}u_j\mathbf{e_i} \tag{2.2}$$

Here, v_i and u_i are respectively the components of $\mathbf{v}$ and $\mathbf{u}$, and S_{ij} are the components of the tensor $\mathbf{S}$.

If the vectors $\mathbf{u}$ and $\mathbf{v}$ are expressed in a new Cartesian coordinate system with orthonormal basis vectors $\mathbf{e'_i}$ as $\mathbf{u'}$ and $\mathbf{v'}$ such that $\mathbf{v'} = \mathbf{S'u'}$, their relationship is given by Eq. (2.3).

$$v'_i\mathbf{e'_i} = \left(S'_{ij}\mathbf{e'_i} \otimes \mathbf{e'_j}\right) \cdot (u'_k\mathbf{e'_k}) = S'_{ij}u'_j\mathbf{e'_i} \tag{2.3}$$

Here, v'_i and u'_i are respectively the components of $\mathbf{v'}$ and $\mathbf{u'}$, and S'_{ij} are the components of the tensor $\mathbf{S'}$.

From the expressions of Eq. (2.2) and Eq. (2.3), it is not difficult to establish the relationship between the components of the tensors $\mathbf{S}$ and $\mathbf{S'}$ by using Eq. (2.1) to express v'_i as $v'_i = A_{ik}v_k$ as shown below.

$$A_{i,k}S_{kl}u_l = S'_{ij}u'_j \Rightarrow A_{i,k}S_{kl}A^T_{lj}u'_j = S'_{ij}u'_j \tag{2.4}$$

Thus, from Eq. (2.4), the relationship between two second order tensors expressed in two different Cartesian coordinate systems is given by Eq. (2.5).

$$S'_{i,j} = A_{i,k}S_{kl}A^T_{lj} \text{ or } \mathbf{S'} = \mathbf{ASA^T} \tag{2.5}$$

Here, S'_{ij} and S_{kl} are the components of the tensors $\mathbf{S'}$ and $\mathbf{S}$.

The transformation equations given by Eq. (2.1) and Eq. (2.5) are applicable only to the Cartesian space, which is a special case of the general curvilinear space. Unlike the Cartesian space that is generated from coordinate axes, the curvilinear

space is generated from coordinate curves [12]. The basis vectors $\mathbf{g_i}$ of the curvilinear space are tangent to the coordinate curves and are not necessarily orthogonal to each other [12]. Furthermore, these basis vectors are position dependent unlike the basis vectors of the Cartesian space. One example of curvilinear coordinate system that is commonly used, is the cylindrical coordinate system. The curvilinear coordinates Θ_i of the cylindrical system are the familiar (r, θ, z), which are expressed in terms of the basis vectors $\mathbf{g_i} = (r, \theta, z)$. Although problems are easier to solve in the Cartesian coordinate systems, many problems do not lend themselves to a treatment in this simple system and require one to work within the framework of the curvilinear space [12]. This is particularly valid for the broad problem of interest to this dissertation work; that is, the redirection of waves, whereas the shape of the domains of interest are often not suited for the Cartesian coordinate system. Consequently, it is necessary to establish the coordinate transformation rules for the curvilinear space. The author presents these rules in Eq. (2.8) and Eq. (2.9) without a rigorous mathematical treatment.

Let one have two curvilinear coordinate systems Θ_i and Θ'_i, which are related to each other. The basis vectors at a position $\mathbf{X}$ for the two coordinate systems are given by Eq. (2.6) [3, 12].

$$\mathbf{g_i} = \frac{\partial \mathbf{X}}{\partial \Theta_i} \text{ and } \mathbf{g'_i} = \frac{\partial \mathbf{X}}{\partial \Theta'_i} \tag{2.6}$$

By using the chain rule, the two basis vectors can be related as shown in Eq. (2.7).

$$\mathbf{g_i} = \frac{\partial \Theta'_j}{\partial \Theta_i}\frac{\partial \mathbf{X}}{\partial \Theta'_j} = \frac{\partial \Theta'_j}{\partial \Theta_i}\mathbf{g'_j} \text{ and } \mathbf{g'_i} = \frac{\partial \Theta_j}{\partial \Theta'_i}\frac{\partial \mathbf{X}}{\partial \Theta_j} = \frac{\partial \Theta_j}{\partial \Theta'_i}\mathbf{g_j} \tag{2.7}$$

Since the expression in Eq. (2.7) relates the basis vectors of two curvilinear coordinate systems, it is not difficult for one to establish the transformation rules for a vector $\mathbf{u}$ by expressing it in terms of the basis vectors in each system. This leads to Eq. (2.8), the transformation rule for vector in curvilinear space [3, 12].

$$u'_i = u_j \frac{\partial \Theta'_i}{\partial \Theta_j} = F_{ij} u_j \tag{2.8}$$

Here, $F_{ij} \coloneqq \frac{\partial \Theta_i}{\partial \Theta'_j}$ are the components of the deformation gradient tensor $\mathbf{F}$.

The transformation rule for tensor quantities in curvilinear coordinate systems can be derived in the similar way as before for Cartesian coordinate systems by using Eq. (2.7) and Eq. (2.8). This is given below by Eq. (2.9)[3, 12].

$$S'_{ij} = \frac{\partial \Theta'_i}{\partial \Theta_k}\frac{\partial \Theta'_j}{\partial \Theta_p} S_{kp} = F_{ik} F_{jp} S_{kp} \tag{2.9}$$

Here, $F_{ij} \coloneqq \frac{\partial \Theta_i}{\partial \Theta'_j}$ are the components of the deformation gradient tensor $\mathbf{F}$.

Let one considers a mapping that takes a reference configuration of a body Ω to a deformed configuration Ω_x. The mapping $\mathcal{X} \longrightarrow \mathbf{x}$ takes points $(\mathcal{X})$ from Ω to points (x) in Ω_x as shown in Figure 2.1. The Jacobian of the mapping is given by Eq. (2.10) [11].

$$J = \det(\mathbf{F}) \tag{2.10}$$

Here, $F_{ij} \coloneqq \frac{\partial x_i}{\partial \mathcal{X}_i}$ are the components of the deformation gradient tensor $\mathbf{F}$.

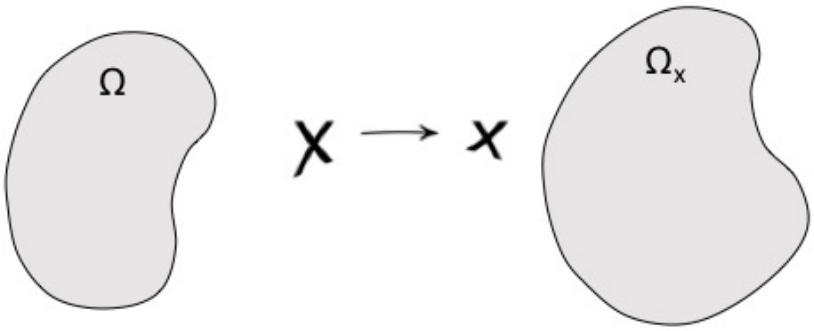

Figure 2.1: Body mapped from reference configuration Ω to deformed configuration Ω_x through mapping $\mathcal{X} \longrightarrow \mathbf{x}$.

The Maxwell's equations in the original and deformed configuration ($\mathcal{X}$) and (x) are given respectively by Eq. (2.11) and Eq. (2.12).

$$\begin{aligned} \nabla_{\mathcal{X}} \times \mathbf{E} + \boldsymbol{\mu} \frac{d}{dt} \mathbf{H} = 0 \\ \nabla_{\mathcal{X}} \times \mathbf{H} - \boldsymbol{\epsilon} \frac{d}{dt} \mathbf{E} = 0 \end{aligned} \tag{2.11}$$

Here, $\mathbf{E}$ and $\mathbf{H}$ are the electrical and magnetic field vectors. In addition, $\boldsymbol{\mu}$ and $\boldsymbol{\epsilon}$ are respectively the magnetic permeability and electric permittivity tensors.

$$\begin{aligned} \nabla'_x \times \mathbf{E}' + \boldsymbol{\mu}' \frac{d}{dt} \mathbf{H}' = 0 \\ \nabla'_x \times \mathbf{H}' - \boldsymbol{\epsilon}' \frac{d}{dt} \mathbf{E}' = 0 \end{aligned} \tag{2.12}$$

Here, $\mathbf{E}'$ and $\mathbf{H}'$ are the electrical and magnetic field vectors. And $\boldsymbol{\mu}'$ and $\boldsymbol{\epsilon}'$ are respectively the magnetic permeability and electric permittivity tensors.

In Eq. (2.11) and Eq. (2.12), the electrical and magnetic field vectors $\mathbf{E}'$ and $\mathbf{H}'$ transform according to the coordinate transformation rules for vectors; that is, Eq. (2.8). Similarly, the magnetic and electric permittivity tensors $\boldsymbol{\mu}$ and $\boldsymbol{\epsilon}$ transform according to Eq. (2.9). One can demonstrate by using the aforementioned transformation rules that the permittivity and permeability tensors are given by Eq. (2.13).

$$\begin{aligned} \boldsymbol{\mu}'(\mathbf{x}) &= \frac{\mathbf{F} \cdot \boldsymbol{\mu}(\mathcal{X}) \cdot \mathbf{F}^{\mathbf{T}}}{\det \mathbf{F}} \\ \boldsymbol{\epsilon}'(\mathbf{x}) &= \frac{\mathbf{F} \cdot \boldsymbol{\epsilon}(\mathcal{X}) \cdot \mathbf{F}^{\mathbf{T}}}{\det \mathbf{F}} \end{aligned} \tag{2.13}$$

The mapping relationship of the permeability and permittivity tensors $\boldsymbol{\mu}$ and $\boldsymbol{\epsilon}$ from a reference configuration to a deformed configuration; that is, Eq. (2.11) and Eq. (2.12), are the fundamental equations of what is known today as transformation electromagnetics.

2.1.2 Methodology and Applications

The invariance of the Maxwell's equations, as illustrated in Eq. (2.11) and Eq. (2.12), was long established. However, it is Pendry that recognized the usefulness of the invariance characteristics of the equations to the formulation of devices that can be used to redirect electromagnetic waves. Indeed, in a seminal paper, Pendry shows that Eq. (2.13) can be used to formulate the material properties of devices that would guide electromagnetic waves in a manner analogus to the physical deformation

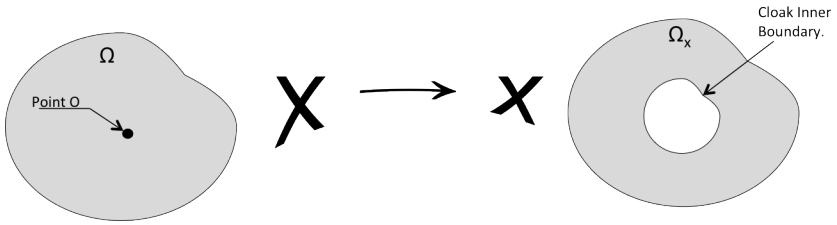

Figure 2.2: Singular transformation for cloaking.

achieved by the mapping $\mathcal{X} \longrightarrow \mathbf{x}$ [8]. As an application of his insightful discovery, Pendry suggested that a cloaking device can be formulated by using a mapping $\mathcal{X} \longrightarrow \mathbf{x}$, which stretches a point (O) of a two-dimensional or three-dimensional finite reference domain Ω to the outer boundary of a two-dimensional or three-dimensional hole on the same finite domain in a deformed configuration as shown in Figure 2.2 [8]. As a demonstration, Pendry used the cylindrical coordinate mapping $(r, \theta, \phi) \rightarrow (r', \theta', \phi')$ given by Eq. (2.14) to formulate the parameters of a spherical cloak by using Eq. (2.13) [8].

$$\begin{aligned} r' &= R_1 + r\frac{R_2 - R_1}{R_2} \\ \theta' &= \theta \\ \phi' &= \phi \end{aligned} \tag{2.14}$$

Here, (r, θ, ϕ) are the spherical coordinates in the reference domain, and (r', θ', ϕ') are the spherical coordinates in the deformed domain. R_1 and R_2 are the inner and outer radii of the cloaking device.

The ensuing parameters of the spherical electromagnetic cloak can be found from the mapping given by Eq. (2.14). These are given by Eq. (2.15).

$$\boldsymbol{\mu}' = \boldsymbol{\mu} \begin{bmatrix} \frac{R_2}{R_2-R_1}\frac{(r'R_1)^2}{r'} & 0 & 0 \\ 0 & \frac{R_2}{R_2-R_1} & 0 \\ 0 & 0 & \frac{R_2}{R_2-R_1} \end{bmatrix}$$

$$\boldsymbol{\epsilon}' = \boldsymbol{\epsilon} \begin{bmatrix} \frac{R_2}{R_2-R_1}\frac{(r'R_1)^2}{r'} & 0 & 0 \\ 0 & \frac{R_2}{R_2-R_1} & 0 \\ 0 & 0 & \frac{R_2}{R_2-R_1} \end{bmatrix} \tag{2.15}$$

The equations of transformation electromagnetics, Eq. (2.13), were extended to acoustics by using the analogy between the two-dimensional single polarization Maxwell's equations and the two-dimensional acoustic wave equations [13, 14]. The material properties for transformations acoustics; that is, the density $\boldsymbol{\rho}$ and the bulk modulus β were derived and are given by Eq. (2.16).

$$\begin{aligned} \boldsymbol{\rho}'(\mathbf{x}) &= \frac{\mathbf{F}\cdot\boldsymbol{\rho}(\mathcal{X})\cdot\mathbf{F}^{\mathbf{T}}}{\det\mathbf{F}} \\ \frac{1}{\beta'(\mathbf{x})} &= \frac{1}{\beta(\mathcal{X})}\frac{\mathbf{F}\cdot\mathbf{F}^{\mathbf{T}}}{\det\mathbf{F}} \end{aligned} \tag{2.16}$$

The expressions of Eq. (2.16) were used to formulate the parameters of two-dimensional acoustic cylindrical cloaks by taking advantage of the cylindrical coordinate mapping $(r, \theta, z) \rightarrow (r', \theta', z')$ given by Eq. (2.17) [13, 14].

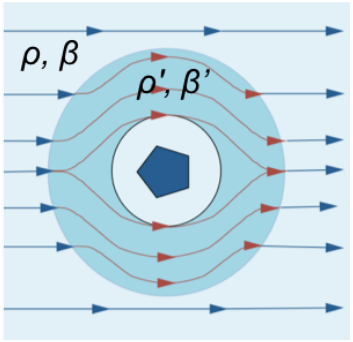

Figure 2.3: Two-dimensional infinite circular acoustic cloak concept.

$$\begin{aligned} r' &= R_1 + r\frac{R_2 - R_1}{R_2} \\ \theta' &= \theta \\ z' &= z \end{aligned} \tag{2.17}$$

Here, (r, θ, z) are the cylindrical coordinates in the reference domain, and (r', θ', z') are the cylindrical coordinates in the deformed domain. R_1 and R_2 are the inner and the outer radii of the cloaking device.

From Eq. (2.17) and by using Eq. (2.16), one can find the parameters of the two-dimensional circular acoustic cloak. This is given in Eq. (2.18) [13, 14]. In Figure 2.3, the author illustrates the concept of a two-dimensional acoustic cloak of circular cross section.

$$\boldsymbol{\rho'} = \boldsymbol{\rho} \begin{bmatrix} \frac{r}{r-R_1} & 0 \\ 0 & \frac{r-R_1}{r} \end{bmatrix} \tag{2.18}$$

$$\beta' = \frac{1}{\beta}\frac{R_2^2}{(R_2 - R_1)^2}\frac{r - R_1}{r}$$

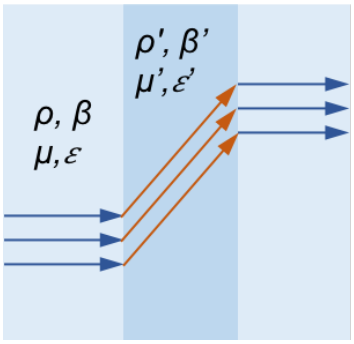

Figure 2.4: Two-dimensional infinite beam shifting device concept.

The above discussion underscored the application of the transformation approach to the formulation of cloaking devices. However, the method is applicable to the formulation of other devices as long as one can find the necessary transformation. A simple illustration is the formulation of a two-dimensional device that can be used to shift an incident beam. The author illustrates this concept in Figure 2.4. Using Eq. (2.13) or Eq. (2.16) one can find the properties of the beam shifting device of Figure 2.4 by using the Cartesian coordinate mapping $(x, y, z) \rightarrow (x', y', z')$ of Eq. 2.19 [5, 15]. These properties are given by Eq. (2.20) for the acoustic case [5].

$$\begin{aligned} x' &= x \\ y' &= y' + \frac{b}{a}x' \\ z' &= z \end{aligned} \tag{2.19}$$

Here, a is the thickness of the device and b is the vertical shift of the incident beam.

$$\boldsymbol{\rho}' = \boldsymbol{\rho} \begin{bmatrix} 1 + (\frac{b}{a})^2 & (\frac{-b}{a}) & 0 \\ (\frac{-b}{a}) & 1 & 0 \\ 0 & 0 & 1 \end{bmatrix} \tag{2.20}$$

$$\beta' = \beta$$

2.1.3 Summary

In this chapter, the author introduced the mathematical foundations of the transformation approach to wave redirection. The author discussed the methodology and its applications for the formulation of wave redirection devices for both electromagnetic and acoustic waves. Although, emphasis is put on cloaking, the transformation method can be used for formulating other devices for wave redirection. The author illustrated this by presenting the case of a simple device for shifting incident beams. To date, the transformation method have been used to formulate practical devices such as cloaking, focusing, and beam shifting devices; to list only a few [5, 16]. In the next chapter, the author will present his efforts to formulate a sequence of transformations that can be useful to cloaking airfoil geometries.

Chapter 3: Transformations Sequence for Cloaking Airfoil Sections

3.1 Overview

In the previous chapter, a review of the transformation approach for formulating devices capable of bending waves for practical applications was presented. Amongst the applications, the formulation of cloaking devices has been the most sought-after application to date. Cloaking has tremendous implications, and the transformation method brought the long time human reverie of designing invisibility cloaks within the realms of realization for the first time. As presented in Chapter 2, the construction of an invisibility cloak by using the transformation method consists of exploiting a change of coordinates to create a void region within a finite space whilst keeping the outer boundary of the considered space unchanged [8]. From the ensuing transformation equations, the properties of an invisibility cloak can then be inferred by using existing formulae; for example, Eq. (2.13) for electromagnetics and Eq. (2.16) for acoustics [14]. To date, the approach has been successfully applied to two-dimensional geometries such as circular and square cylinders by determining the necessary transformations equations [13, 15]. In this chapter, the author summarizes an effort to derive transformations equations that can be exploited for cloaking two-dimensional airfoil sections by using the transformation method.

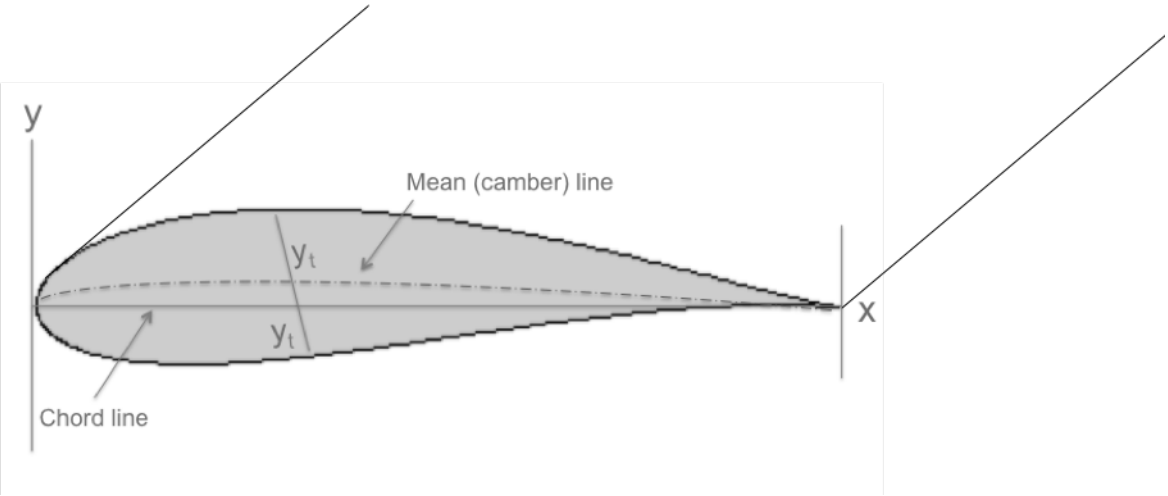

Figure 3.1: Airfoil geometry.

An airfoil is a two-dimensional geometry that is representative of the cross section of an aircraft wing, or similarly shaped structures. In Figure 3.1, the author illustrates a basic airfoil section with its principal elements and dimensions shown. The chord line is the straight line connecting the leading and the trailing edges of the airfoil. The mean camber line is the locus of point midway between the top and bottom surfaces of the airfoil [17, 18]. Airfoils originated from the aerospace field, where an understanding of the flow around their shape played a fundamental role in the development of airplanes. Throughout the years, many airfoils sections were developed and tested around the world. This led to various families of airfoils including NACA airfoils, a family developed in the United States by the National Committee for Aeronautics (NACA) [17, 18]. NACA airfoils are the most commonly used airfoils for wing sections, and are obtained from the addition of a thickness distribution to a camber line [17, 18]. For instance, the simplest NACA series,

the four-digit NACA-ABCD, is obtained by using the thickness distribution y_t and leading edge radius r_t given by the polynomial expressions of Eq. (3.1) [17, 18].

$$\begin{aligned} \pm y_t &= \frac{t}{0.2}(0.29690\sqrt{x} - 0.12600x - 0.35160x^2 + 0.28430x^3 - 0.10150x^4) \\ r_t &= 1.1019t^2 \end{aligned} \tag{3.1}$$

In the four-digit designation, the digits A, B, C, and D provide the following information about the airfoil [17, 18].

- The first integer A indicates the maximum value of the mean-line ordinate as a percentage of the chord.
- The second integer B indicates the distance from the leading edge to the location of the maximum camber as tenth of the chord.
- The last two integers CD indicate the section thickness as a percentage of the chord.

As an example, NACA 2420 is an airfoil section that has a 2 percent camber located at 0.4 chord length from the leading edge and a thickness of 20 percent of the chord. Note that symmetric airfoils are represented by using zeros for the two first digits in the designation [17]. Thus NACA 0030 is a symmetric airfoil with a thickness that is 30 percent of the chord length.

Apart from aircraft wing designs, airfoil geometries are also encountered in seaborne vehicles such as submarines where they typically serve as diving aides or stabilizing structures. Thus, airfoils are prevalent on vehicles that operate in both

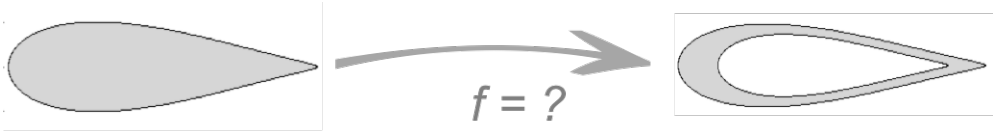

Figure 3.2: Mapping of airfoil disc to airfoil annulus.

RADAR and SONAR environments; that is, airplanes and submarines. This makes the problem of cloaking airfoil geometries relevant to both electromagnetics and acoustics. In the present investigation, the author aspires to find a sequence of transformations that can be used to formulate electromagnetic and acoustic airfoil cloaks. Consistent with the premise of the transformation method, a transformation f is sought that can be used to map an airfoil disc to an airfoil annulus as illustrated in Figure 3.2.

To solve the problem of finding transformation f, the author took the approach of breaking it down to the simpler problem of finding a sequence of three transformations f_1, f_2, and f_3 as illustrated in Figure 3.3. The first transformation f_1 can be used to map an airfoil disc to a circular disc. The circular disc can then be mapped to a circular annulus by using transformation f_2. Finally, transformation f_3 can be used to map the circular annulus to an airfoil annulus with the same outer boundary as the original airfoil disc. Once all three transformations are found, the sought-after transformation f can be determined by using their composition. The motivation of the aforementioned approach is to take advantage of the mapping properties of the Joukowski and Karman-Trefftz transformations, two complex variable maps that are classically used to approximate airfoils in aerodynamics applications [19, 20]. This would become more evident in the remaining of this chapter, which is organized

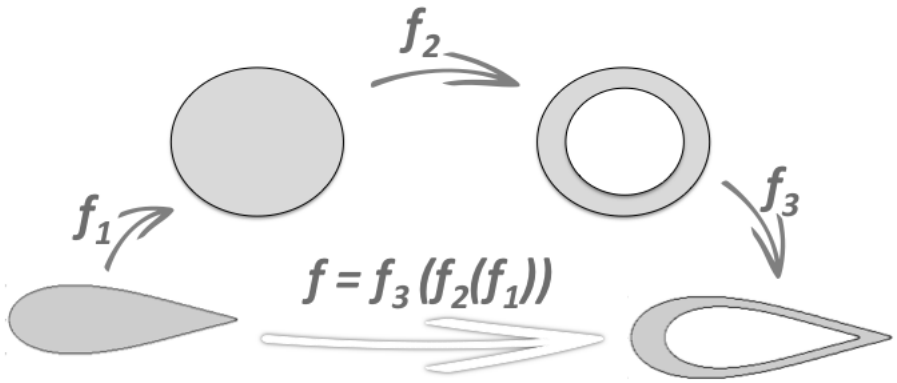

Figure 3.3: Mapping sequence of airfoil to annular airfoil.

as follow. In the next section, the author briefly introduces the Joukowski and the Karman-Trefftz transformations and their relevant mapping properties to the problem of interest. In subsequent sections, the author presents his efforts to determine the sought-after transformation f by solving for the three transformation f_1, f_2, and f_3. The found transformations are discussed in the context of formulating airfoil cloaks by using the transformation method.

3.2 Transformations for Cloaking Airfoil Geometries based on the Joukowski and Karman-Trefftz Transformations

3.2.1 The Joukowski Transformation

The important role that the study of flow around airfoil geometries played in flight theory and the development of aircraft wing cannot be overstated. However, at a time when computers were not available, obtaining accurate results for the flow around these complex geometries was a very daunting tasks that required solving

Laplace's equation over their surfaces [20]. This difficulty was overcome by the Russian mathematician and aerodynamicist Nikolai Joukowski in a pioneering work in 1914 [17]. Joukowski exploited the method of conformal mapping [21, 22] to derive transformations that led to the exact analytical solution of the flow around some airfoil geometries by using Laplace's equation and the known solution to the flow around circles [20, 21]. In its general form, the Joukowski transformation is a complex conformal mapping given by Eq. (3.2). For various choices of the parameter λ, the Joukowski transformation maps a circle centered at the origin and with radius $r \geq 1$, to various geometries; this includes a line segment and an ellipse as illustrated in Figure 3.4.

$$w(z) = \frac{1}{2}\left(z + \frac{\lambda^2}{z}\right) \tag{3.2}$$

Here z and w represents points respectively in the complex z- and w-plane. The parameter λ is the transformation parameter.

However, for a circle slightly off-centered from the origin to a new center (a, b), the Joukowski transformation yields shapes similar to that of an airfoil for choices of the paramater λ such that $\lambda = r - |s|$, with $s = a + ib$, as shown in Figure 3.5 [20]. The generated airfoils are referred to as Joukowski airfoils and are characterized by a cusp at the trailing end. Note that the Joukowski transformation cannot exactly yield standard airfoils from the NACA family. However, with the proper choice of parameters, a close approximation to specific NACA airfoils can be achieved. It should also be mentioned that the Joukowski transformation is invertible and its

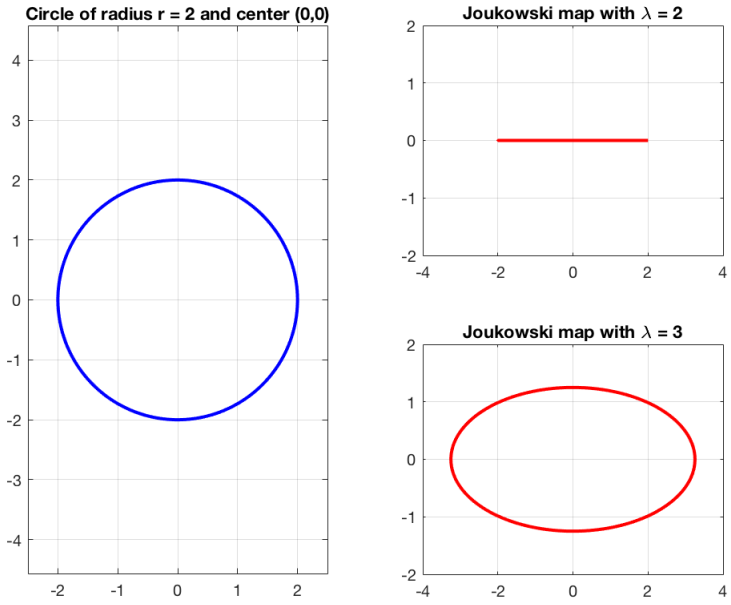

Figure 3.4: Joukowski mapping of circle centered at origin with parameter λ.

inverse is a multivalued complex function with two branch cuts as shown in Eq. (3.3) [23].

$$z(w) = w \pm \sqrt{w^2 - \lambda^2} \tag{3.3}$$

3.2.2 Karman-Trefftz Transformation

As discussed above, the Joukowski transformation was of tremendous use in the early studies of flows around airfoils. The simplicity of both the transformation and its inverse makes it an attractive first choice for approximating airfoils even today. However, the Joukowski transformation presents the undesirable feature of a zero trailing edge angle (cusp), which is uncharacteristic of practical airfoils. Furthermore, the Joukowski transformation only allows two possibilities for modifying

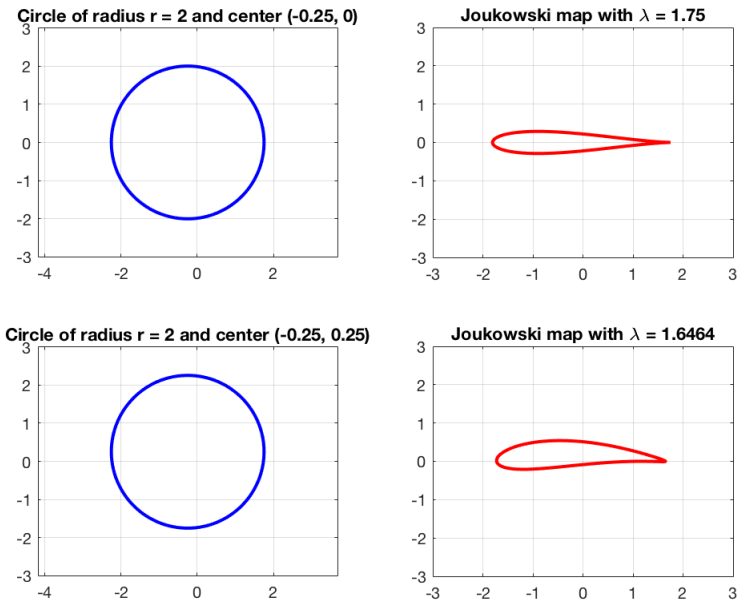

Figure 3.5: Joukowski mapping of circle of radius r and center $s = a+ib$ with parameter $\lambda = r-|s|$.

the profile of an airfoil; that is, the camber and the thickness. To address the aforementioned limitations, Karman and Trefftz introduced a generalized mapping function of the Joukowski transformation that is more versatile in approximating the profile of practical airfoil including NACA families of airfoils [24]. The expression for the Karman-Trefftz transformation is given below by Eq.3.4.

$$w(z) = \lambda b \frac{(z+b)^{\lambda} + (z-b)^{\lambda}}{(z+b)^{\lambda} - (z-b)^{\lambda}} \tag{3.4}$$

As before, z and w represents points in the complex z- and w-planes. The parameter λ and b are the transformation parameters.

Though a more complex expression, the Karman-Trefftz transformation has a number of advantageous characteristics over the Joukowski transformation for approximating airfoils. The most notable difference is the ability for one to specify the

trailing edge angle θ of the airfoil, and subsequently choose the necessary mapping parameter λ according to Eq. (3.5). Note from the expression of Eq. (3.5), that when the trailing edge is chosen to be zero; that is, $\theta = 0$ *degrees*, the mapping parameter $\lambda = 2$. It is not difficult to show in that case that the Karman-Trefftz transformation reduces to the Joukowski transformation [24].

$$\lambda = 2 - \frac{\theta}{180} \tag{3.5}$$

Here, θ is the trailing edge angle in degrees.

Similar to the Joukowski transformation, the Karman-Trefftz transformation maps circles to various airfoil geometries. The transformation parameter b is the critical point when $z = 0$; that is, where the circle of interest intersects the positive real axis in the z-plane. As illustrated in Figure 3.6, a circle centered at the origin yields a symmetric Karman-Trefftz airfoil bounded by two circular arcs. A camber can be introduced to the airfoil by moving the center of the circle along the imaginary axis as shown in the figure [24].

In order to approximate more conventional airfoils, such as symmetric 4-digit series NACA airfoils, one needs to move the center of the circle in the mapping domain (z-plane) on the real negative axis as shown in Figure 3.7. Here again, a camber can be introduced to the airfoil by moving the center of the circle on the second quadrant of the z-plane as with the Joukowski airfoils (see Figure 3.7)[24].

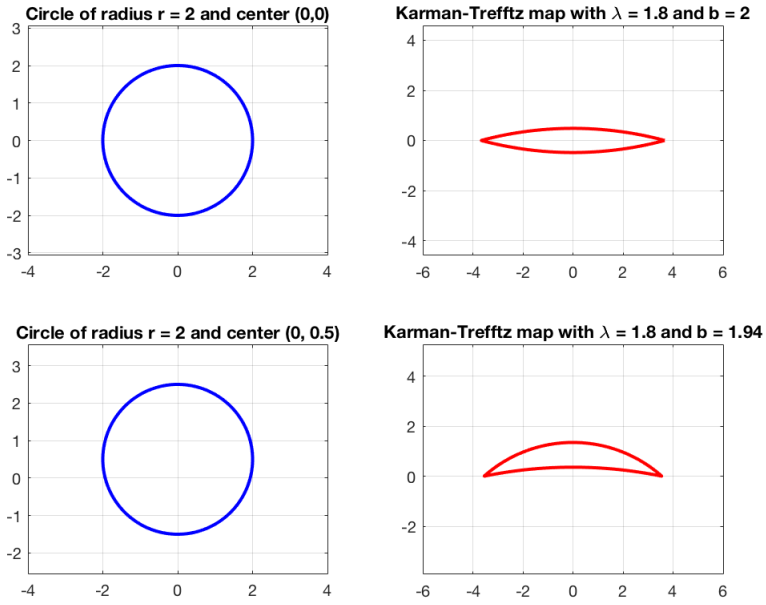

Figure 3.6: Karman mapping of circle centered at origin with trailing edge angle $\theta = 30$ degrees.

3.2.3 Transformations Solutions based on the Joukowski Transformation

In the previous section, the author introduced the Joukowski transformation and its mapping properties for the approximation of airfoils. In particular, the ability to use the transformation to map circles to airfoil profiles was underscored. This characteristic was the main motivation for the choice of the transformations sequence presented in Figure 3.3. As presented in Chapter 2, in the sequence of Figure 3.3, transformation f_2 that can be used to map a circular disc to a circular annulus is already known. This transformation is given by Eq. (2.14), and is reproduced below as Eq. (3.6). Transformation f_2 is illustrated in Figure 3.8 for a disc of radius $R_{out} = 3$, and an annulus of outer and inner radii $R_{out} = 3$ and

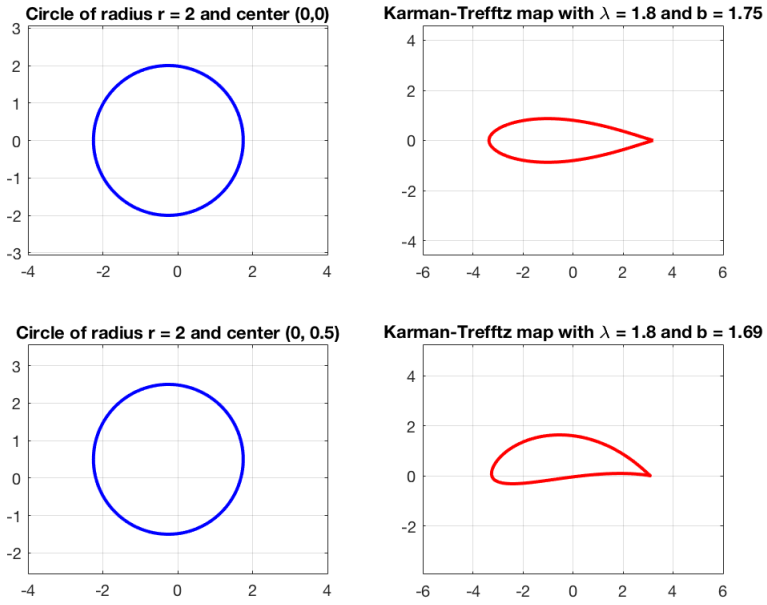

Figure 3.7: Karman mapping of circle of radius r, centered at $s = a + ib$, and with trailing edge angle $\theta = 30$ degrees.

$R_{in} = 2$.

$$\begin{aligned} R_a(R_{cd}) &= R_{out} + \left(\frac{R_{out} - R_{in}}{R_{out}}\right) R_{cd} \\ \Theta_a &= \Theta_{cd} \end{aligned} \tag{3.6}$$

Here, (R_a, Θ_a) is the polar coordinate of a point on the circular disc. Similarly, (R_{cd}, Θ_{cd}) is the polar coordinate of a point on the circular annulus.

Thus, to determine the sought-after transformation f, the task at hand is to find the two transformations f_1 and f_3. To that end, the author chose to first seek f_3, the transformation of a circular annulus to an airfoil shaped annulus in order to take advantage of the mapping properties of the Joukowski transformation. Before proceeding, it needs to be emphasized that the Joukowski transformation, even with

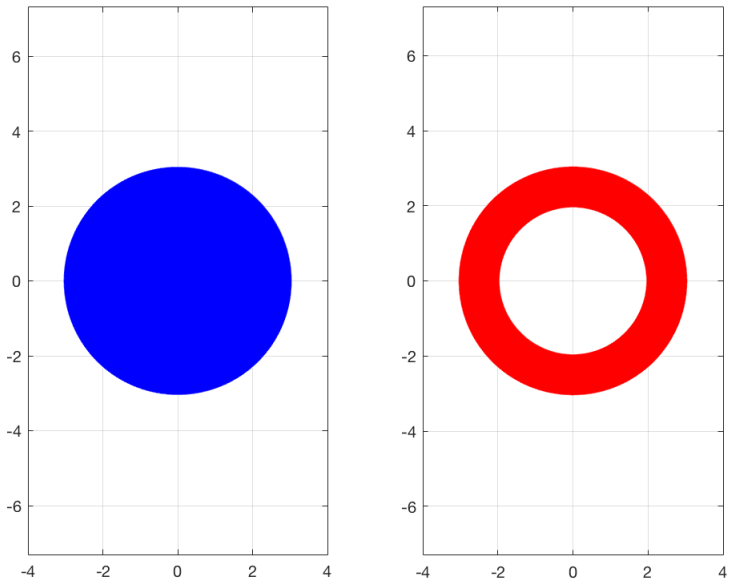

Figure 3.8: Mapping of circular disc centered at origin and of radius $R = 3$ to annulus of outer radius $R_{out} = 3$ and inner radius $R_{in} = 2$.

appropriately chosen parameters, only maps the boundary of a circle in the z-plane to that of an airfoil in the w-plane [25, 26]. The interior points of the circle are mapped to points exterior to the airfoil [25, 26]. Consequently, for one to exploit the mapping properties of the Joukowski transformation and determine f_3 is not a trivial task. This requires careful approach. The author successfully achieved this objective by using a sequence of simple transformations as summarized next.

Let one start with a circular annulus of outer radius R_{out} and inner radius R_{in} centered at the origin $(0, 0)$. Two dimensional mappings are best treated in the complex domain, and the aforementioned annulus has the complex representation of Eq. (3.7). A Cartesian representation of the annulus is also given by Eq. (3.8). Cartesian representations are provided through the derivation steps of f_3 to correlate

each step to the points (x_a, y_a) of the initial circular annulus and underscore the intermediate nature of the transformations.

$$Z_a = x_a + iy_a \quad \text{with } R_{in} \leq |Z_a| = \sqrt{x_a^2 + y_a^2} \leq R_{out} \tag{3.7}$$

$$x_a^2 + y_a^2 = R_a^2 \quad \text{whith } R_{in} \leq R_a \leq R_{out} \tag{3.8}$$

Here, x_a and y_a are the Cartesian coordinates of points on the annulus, and R_a is the radial distance from the origin to a point (x_a, y_a) on the annulus.

Next, the annulus can be mapped to a circle of radius ρ centered at the origin by projecting the points on the unit circle, which can then be scaled to a circle of radius ρ. This is achieved by dividing the complex representation of each point on the annulus, Eq. (3.7), by the corresponding magnitude and then multiplying by ρ. The result, which is shown in the complex representation, Eq. (3.9), is illustrated in Figure 3.9 for a circle of radius $\rho = 2$, and an annulus with an outer radius $R_{out} = 3$ and inner radius $R_{in} = 2$. The mapping of Eq. (3.9) can be expressed as function of the coordinate points (x_a, y_a) as shown in the Cartesian representation of Eq. (3.10).

$$Z_c = \rho \frac{Z_a}{|Z_a|} \tag{3.9}$$

$$\begin{aligned} x_c &= \frac{\rho x_a}{\sqrt{x_a^2 + y_a^2}} \\ y_c &= \frac{\rho y_a}{\sqrt{x_a^2 + y_a^2}} \end{aligned} \tag{3.10}$$

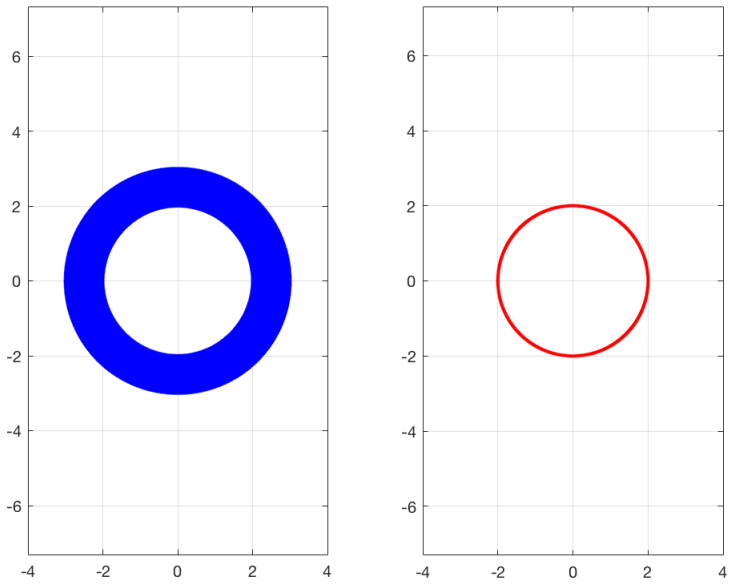

Figure 3.9: Mapping of annulus centered at origin, and of outer radius $R_{out} = 3$ and inner radius $R_{in} = 2$ to circle of radius using Eq. (3.9)

Here, x_c and y_c are the Cartesian coordinates of the projected points on the circle of radius ρ.

With the circular annulus transformed to a circle centered at the origin, one can take advantage of the the mapping properties of the Joukowski transformation to obtain an airfoil profile. However, to do so, the center of the circle of Eq. (3.9) needs to be shifted from the origin to a point s with Cartesian coordinates (α, β). This leads to the new circle given by the expression of Eq. (3.11), and is illustrated in Figure 3.10 for the circle of Figure 3.9. Again, the Cartesian representation of Eq. (3.12) relates a point (x_{cs}, y_{cs}) on the circle to a point (x_a, y_a) on the starting circular annulus.

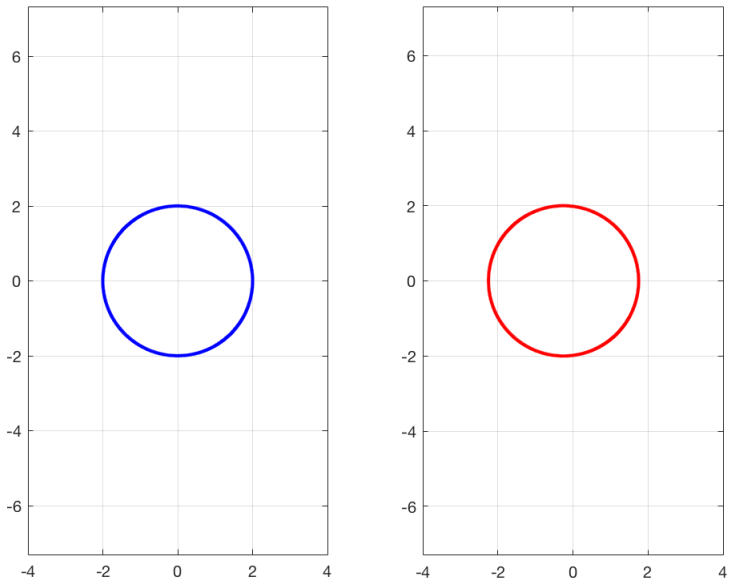

Figure 3.10: Mapping of circle centered at origin and of radius $\rho = 2$ to circle of same radius, but centered at $s(-0.25, 0)$ by using Eq. (3.11).

$$Z_{cs} = Z_c + s \quad \text{with } Z_{cs} = x_{cs} + iy_{cs}, \text{ and } s = \alpha + i\beta \tag{3.11}$$

$$\begin{aligned} x_{cs} &= \frac{\rho x_a + \alpha\sqrt{x_a^2 + y_a^2}}{\sqrt{x_a^2 + y_a^2}} \\ y_{cs} &= \frac{\rho y_a + \beta\sqrt{x_a^2 + y_a^2}}{\sqrt{x_a^2 + y_a^2}} \end{aligned} \tag{3.12}$$

Here, x_{cs} and y_{cs} are the Cartesian coordinates of the points on the circle of radius ρ and center $s(\alpha, \beta)$.

The points (x_{cs}, y_{cs}) on the circle of radius ρ and center (α, β) can be mapped to points (x_j, y_j) on the boundary of a Joukowski airfoil by using the Joukowski transformation. To obtain an airfoil, the mapping parameter λ must be restricted such that $\lambda = \rho - |s| = \rho - \sqrt{\alpha^2 + \beta^2}$, as was underscored in the previous section.

The ensuing transformation is given in the complex form as Eq. (3.13), and is illustrated in Figure 3.11 for the circle of Figure 3.10. The Cartesian form of the combined sequence is given by Eq. (3.14).

$$Z_j = \frac{1}{2}\left(Z_{cs} + \frac{\lambda^2}{Z_{cs}}\right) = \frac{1}{2}\left(Z_{cs} + \frac{\lambda^2 \bar{Z}_j}{|Z_{cs}|}\right) \quad \text{with } Z_j = x_j + iy_j \tag{3.13}$$

$$\begin{aligned} x_j &= \frac{1}{2}\left(\frac{\rho x_a + \alpha\sqrt{x_a^2+y_a^2}}{\sqrt{x_a^2+y_a^2}} + \frac{\lambda^2\sqrt{x_a^2+y_a^2}\left(\rho x_a + \alpha\sqrt{x_a^2+y_a^2}\right)}{\left(\rho x_a + \alpha\sqrt{x_a^2+y_a^2}\right)^2 + \left(\rho y_a + \beta\sqrt{x_a^2+y_a^2}\right)^2}\right) \\ y_j &= \frac{1}{2}\left(\frac{\rho y_a + \beta\sqrt{x_a^2+y_a^2}}{\sqrt{x_a^2+y_a^2}} - \frac{\lambda^2\sqrt{x_a^2+y_a^2}\left(\rho y_a + \beta\sqrt{x_a^2+y_a^2}\right)}{\left(\rho x_a + \alpha\sqrt{x_a^2+y_a^2}\right)^2 + \left(\rho y_a + \beta\sqrt{x_a^2+y_a^2}\right)^2}\right) \end{aligned} \tag{3.14}$$

Here, x_j and y_j are the Cartesian coordinates of the points on the Joukowski airfoil profile.

Thus far, the sequence of transformations given by Eq. (3.9) - Eq. (3.14) can be used to map a circular annulus to the profile of a Joukowski airfoil. As can be discerned from Eq. (3.14), each points $Z_j = x_j + iy_j$ on the Joukowski airfoil profile represented by Eq. (3.13) is associated with a point $Z_a = x_a + iy_a$, on the original annulus represented by Eq. (3.7). Since each point Z_a on the annulus was first projected on the unit circle by scaling by its modulus $|Z_a| = \sqrt{x_a^2+y_a^2}$, one can obtain the sought-after Joukowski airfoil annulus by re-scaling back each point Z_j on the Joukowski airfoil profile of Eq. (3.13) by the modulus $|Z_a|$ associated with it as shown in Eq. (3.15). This transformation is illustrated in Figure 3.12 and concludes the sequence of transformations necessary to find f_3.

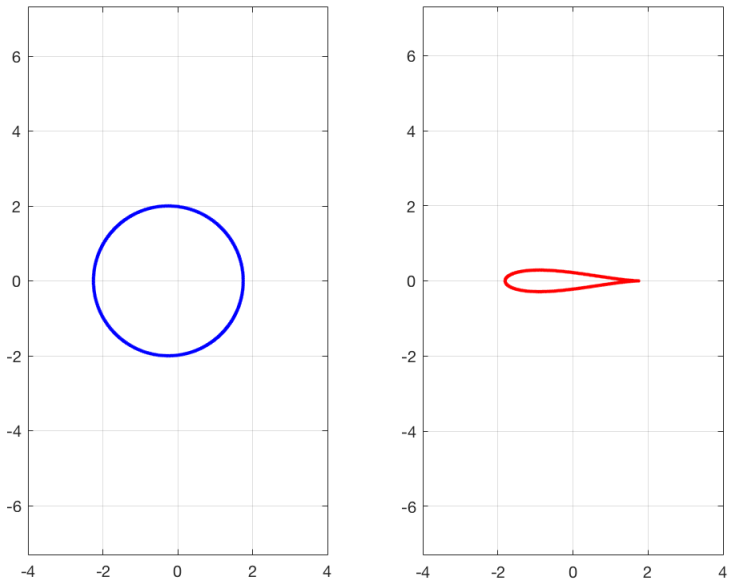

Figure 3.11: Mapping of circle centered at $s(-.25, 0)$ to Joukowski airfoil profile using Eq.3.13.

$$Z_{ja} = |Z_a| Z_j \quad \text{with } Z_{ja} = x_{ja} + i y_{ja} \tag{3.15}$$

Transformation f_3 can be expressed in complex and Cartesian forms respectively as Eq. (3.16), and Eq. (3.17), and can be used to map a point (x_a, y_a) of a circular annulus $R_{in} \leq \sqrt{x_a^2 + y_a^2} \leq R_{out}$ to a point (x_{ja}, y_{ja}) of a Joukowski airfoil annulus. In Figure 3.14, the author illustrates transformation f_3 for the annulus of Figure 3.8 of outer radius $R_{out} = 3$, and inner radius $R_{in} = 2$.

$$Z_{ja} = \frac{|Z_a|}{2} \frac{\left[\rho \left(\frac{Z_a}{|Z_a|}\right) + s\right]^2 + \lambda^2}{\rho \left(\frac{Z_a}{|Z_a|}\right) + s} \tag{3.16}$$

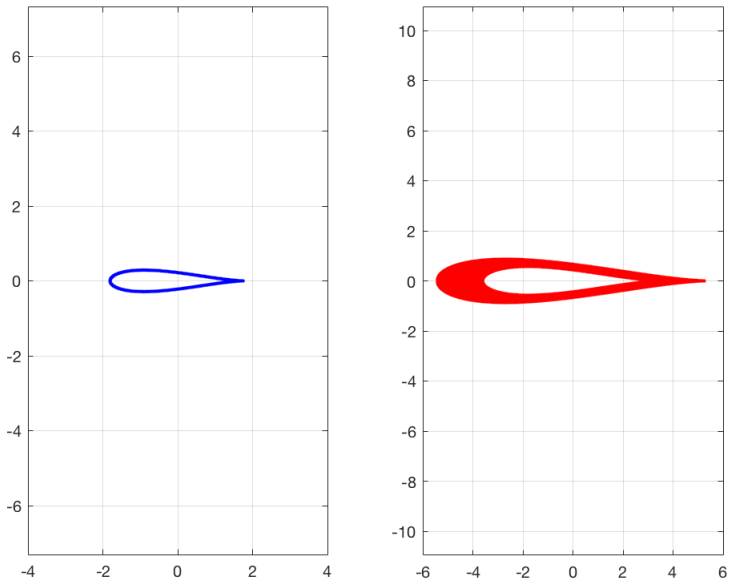

Figure 3.12: Mapping of Joukowski airfoil profile to Joukowski airfoil annulus using Eq. (3.15).

$$x_{ja} = \frac{1}{2}\left(\rho x_a + \alpha\sqrt{x_a^2+y_a^2} + \frac{\lambda^2(x_a^2+y_a^2)\left(\rho x_a + \alpha\sqrt{x_a^2+y_a^2}\right)}{\left(\rho x_a + \alpha\sqrt{x_a^2+y_a^2}\right)^2 + \left(\rho y_a + \beta\sqrt{x_a^2+y_a^2}\right)^2}\right)$$
$$y_{ja} = \frac{1}{2}\left(\rho y_a + \beta\sqrt{x_a^2+y_a^2} - \frac{\lambda^2(x_a^2+y_a^2)\left(\rho y_a + \beta\sqrt{x_a^2+y_a^2}\right)}{\left(\rho x_a + \alpha\sqrt{x_a^2+y_a^2}\right)^2 + \left(\rho y_a + \beta\sqrt{x_a^2+y_a^2}\right)^2}\right) \tag{3.17}$$

Here, the necessary restriction $\lambda = \rho - \sqrt{\alpha^2+\beta^2)}$ is imposed.

Before proceeding with the discussion of the effort to finding f_1, the final transformation needed to determine transformation f, it is worth adjourning to briefly appreciate some features of transformation f_3. In particular, note the explicit and relatively simple nature of f_3 in both complex and Cartesian forms as shown in Eq. (3.7) and Eq. (3.8). Such simple expressions resulted from the relative sim-

plicity of the Joukowski transformation, Eq. (3.2), and can be consequential for formulating cloaking devices. Recall from Chapter 2 that the formulation of wave redirection devices, including cloaking devices, on the basis of the transformation method, requires the calculations of the deformation gradients. These calculations are more manageable tasks analytically, as well as numerically, for explicit expressions such as Eq. (3.7) and Eq. (3.8). Moreover, the deformation gradient of the composition of mapping functions is the product of the deformation gradients of each function. Thus, if one can determine transformation f_1, the deformation gradient of the sought-after function f can be found by calculating the product of the deformation gradients of f_1, f_2, and f_3. Thus far, the transformations f_2 and f_3 are known and their composition $f_3(f_2)$ is demonstrated to map a circular disc to a Joukowski airfoil annulus in Figure 3.13. Next, the author turns to the discussion of the effort of finding transformation f_1 to map a Joukowski airfoil disc to a circular disc as illustrated in Figure 3.3.

The effort to find transformation f_1 has been unsuccessful, and f_1 remains elusive to date. However, a discussion of few of the approaches that the author explored in the unsuccessful effort of finding f_1 is warranted. The discussion underscores the subtleties of the approaches, but also leads to the rationale that led the author to alternatively explore the Karman-Trefftz transformation to determine transformation f in lieu of the Joukowski transformation. By starting with transformation f_3, the author's initial intuition was that transformation f_1 would have been trivial if f_3 was successfully formulated. The insight was that f_1 would have naturally fallen from the above formulation of f_3 as its inverse, but with the inner

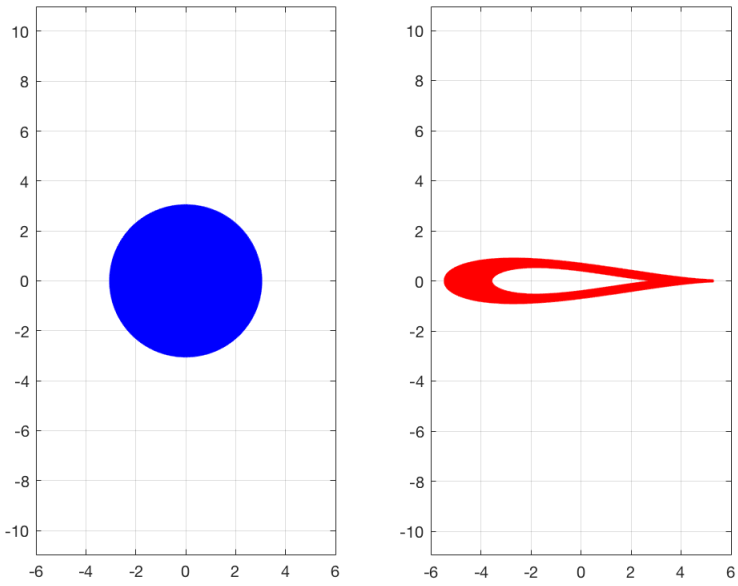

Figure 3.13: Mapping of disc centered at origin and of radius $\rho = 3$ to Joukowski airfoil annulus using composition of f_2 and f_3; that is, $f_3(f_2)$.

radius of the annulus assumed to be approximately equal to zero; that is, $R_{in} \approx 0$. However, it turned out that transformation f_3 is neither invertible at all points nor could an inverse be found ; even numerically by using a powerful symbolic tool such as Mathematica on a personal computer.

The author attributed the difficulties of finding the inverse of f_3 to the cusp at the trailing edge of Joukowski airfoils, and to the fact that the inverse Joukowski transformation of Eq. (3.3) has two branch cuts. Thus, the transformation f_3 is not locally invertible at all points since it is not differentiable at the cusp, nor is the function one-to-one because of the two branch cuts of the inverse. The aforementioned points are two requirements that must be met for a function to be invertible according to the inverse function theorem [27]. Nonetheless, it may be possible that

through mathematical astuteness, an inverse function approach can lead to f_1, by restricting to one branch cut of the inverse Joukowski. This approach was unsuccessful for the author. The vain effort to find transformation f_1 using the inverse function of f_3 and related approaches led the author to explore other avenues. In particular, the author visited the possibility of exploiting other conformal maps to obtain f_1. This stemmed from the Riemann mapping theorem, according to which there exists an analytic bijection (conformal transformation) that can be used to map a simply connected domain in the complex plane $\mathbb{C}$ to the unit disc in $\mathbb{C}$ [28]. To that end, the author opted to circumvent the mathematical difficulties with the Joukowski transformation and explore an approach to finding transformation f based on the more generalized Karman-Trefftz transformation as presented in the following section.

3.3 Transformation Solutions based on the Karman-Trefftz Transformation

In Section 3.2.3 above, the author sought to exploit the mapping properties of the Joukowski transformation to find a sequence of transformations f_1, f_2, and f_3, the composition of which was to give the sought-after transformation f as illustrated in Figure 3.3. In the sequence, transformation f_2 was already known, and the author successfully exploited the mapping properties of the Joukowski transformation to find transformation f_3. However, transformation f_1, which, if formulated, could have been used to map a Joukowski airfoil disc to a circular disc was not successfully

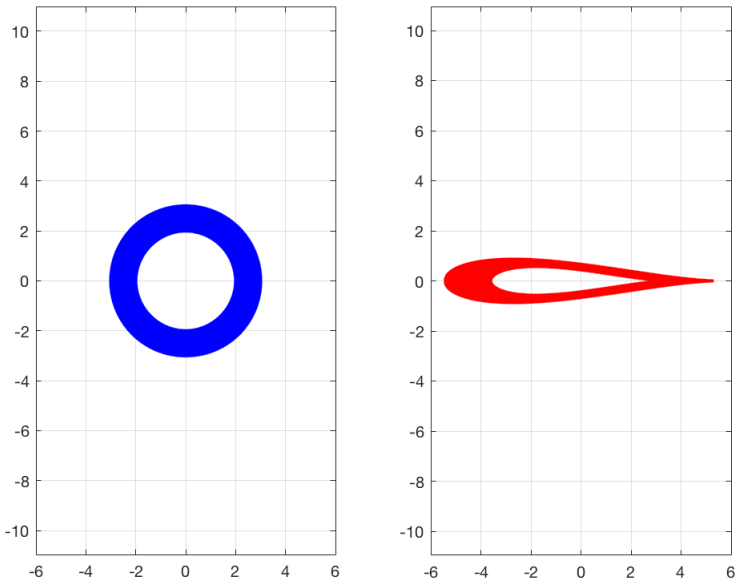

Figure 3.14: Mapping of circle centered at origin and of radius $\rho = 2$ to circle of same radius, but centered at $s(-0,25, 0)$ by using Eq. (3.11).

obtained. As an alternative, the author presents in this section a transformation sequence, the composition can be used to map a symmetric Karman-Trefftz airfoil disc bounded by two circular curves to a Karman-Trefftz airfoil annulus as illustrated in Figure 3.15. To that end, the author exploits the properties of various complex transformations, including the Karman-Trefftz transformation, and leverages the approach he used to finding the transformation f_3 in Section 3.2.3.

To start, let the symmetric Karman-Trefftz airfoil disc of Figure 3.15 be defined by points Z_{ktd} in the complex plane $\mathbb{C}$. The airfoil disc has a chord length C and edge angles α, and its outer profile is a Karman-Trefftz airfoil with paramaters λ and b. The disc can be mapped to an infinite plane bounded by two line segments in the positive half plane, and forming a vertex angle α at the origin. This is achieved by

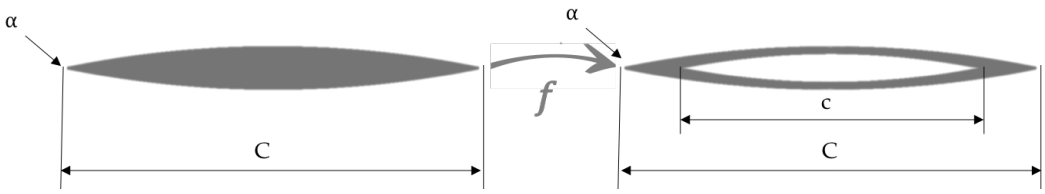

Figure 3.15: Mapping f of a symmetric Karman-Trefftz airfoil disc of chord length C and edge angles α to a Karman-Trefftz airfoil annulus of outer chord C, inner chord c, and edge angles α.

using Eq. (3.18) to map point Z_{ktd} on the disc to a point $Z_{\alpha p}$ on the aforementioned plane. Eq. (3.18) is a linear fractional transformation that maps the upper and lower circular arc boundaries of the airfoil disc to the two line segments bounding the infinite plane and forming a vertex α at the origin [29]. The transformation is illustrated in Figure 3.16.

$$Z_{\alpha p} = \mathrm{e}^{i\pi} \frac{Z_{ktd} + l}{Z_{ktd} + m} \tag{3.18}$$

Here, $l = \lambda b$, and $m = -\lambda b$; with $\lambda = 2 - \frac{\alpha}{\pi}$, and b is such that $C = 2\lambda b$ as defined earlier.

The infinite plane bounded by the two line segments in the positive half space, and with vertex α at the origin can be mapped to the entire positive half space. To do so one needs to use a complex exponentiation as shown in Eq. (3.19) to map points $Z_{\alpha p}$ to points Z_{hp} in the positive half space. The mapping is illustrated in Figure 3.17.

$$Z_{hp} = Z_{\alpha p}^{\frac{\pi}{\alpha}} \tag{3.19}$$

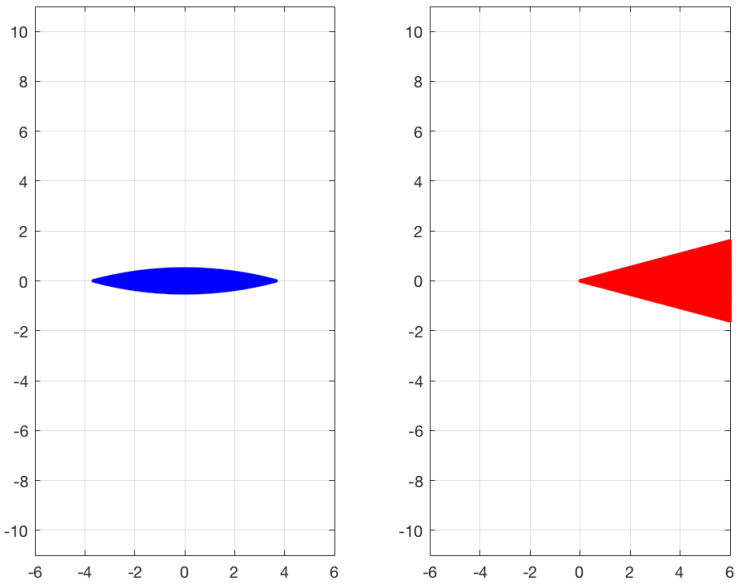

Figure 3.16: Mapping of symmetric Karman-Trefftz airfoil disc of chord length $C = 7.33$ and edge angles $\alpha = \frac{\pi}{6}$ to infinite space bounded by two line segments forming vertex angle $\alpha = \frac{\pi}{6}$ at origin.

To map the positive half space to a circular disc of radius $R_{out} = \lambda b$, one can use Eq. (3.20), which is the inverse of Eq. (3.18). The transformation of Eq. (3.20) is illustrated in Figure 3.18.

$$Z_{cd} = \frac{-m\mathrm{e}^{-i\pi} Z_{hp} + l}{\mathrm{e}^{-i\pi} Z_{hp} - 1} \tag{3.20}$$

Here, l, and m are as defined earlier.

It should be underscored that the sequence of transformations Z_{ktd} through Z_{cd} can be used to map the symmetric Karman-Trefftz airfoil disc shown in Figure 3.15 to a circular disc as shown in Figure 3.18. This is analogous to transformation f_1 in the sequence of Figure 3.3. The logical question may rise as to why such approach was not extended to find the transformation f_1 for a Joukowski airfoil disc. The

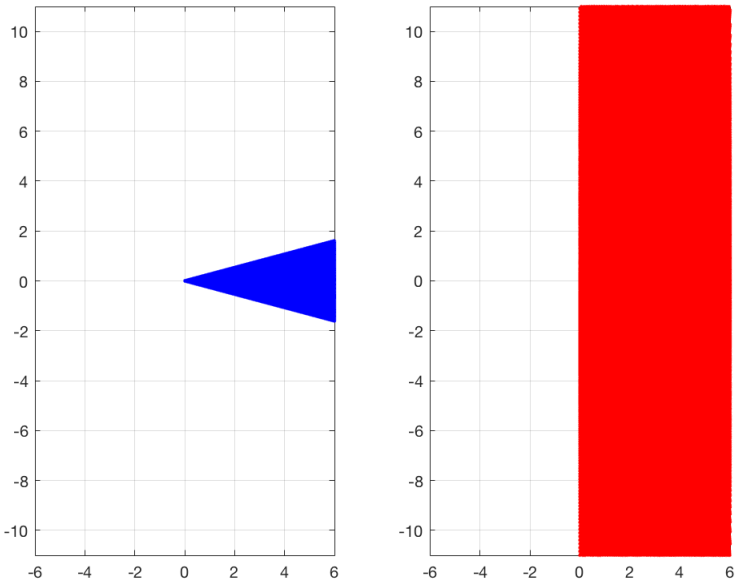

Figure 3.17: Mapping of infinite space bounded by two line segments forming a vertex angle $\alpha = \frac{\pi}{6}$ at origin to infinite positive half space.

reason lies primarily in the undesirable cusp inherent to Joukowski airfoils. The null trailing edge angle does not permit the use of the aforementioned approach since $\alpha \approx 0$ is not compatible with Eq. (3.19). Moreover, the boundaries of Joukowski airfoils are not perfect circular arcs, and this presents a challenge to overcome. A similar challenge is presented by Karman-Trefftz airfoils not bounded by circular curve. The author believes this can be overcome by using complex transformations to relate those Karman-Trefftz airfoils to Karman-Trefftz airfoils bounded by circular arcs. However, the author has not attempted to do so here.

With the sequence of transformations $Z_{\alpha p}$, Z_{hp}, and Z_{cd} determined, the remaining transformations that are needed for one to find the transformation f shown in Figure 3.15 are trivial. Since transformation f_2 of a circular disc to an annulus is

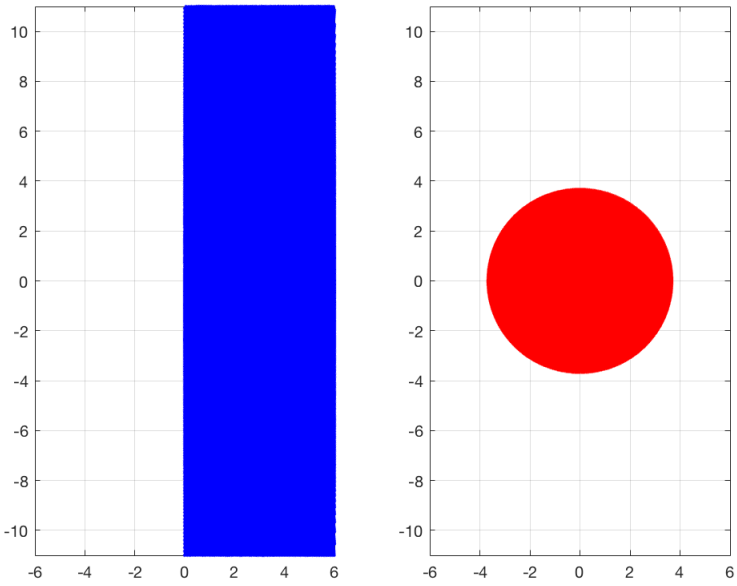

Figure 3.18: Mapping of infinite positive half space to circular disc centered at origin and of radius $R = 3.67$.

already known and given by Eq. (3.6), one can simply use the approach that led to transformation f_3 in Section 3.2.3 to complete the sequence as presented next.

The points Z_{cd} of the disc of radius $R_{out} = \lambda b$ can be mapped to the points Z_a of a circular annulus of outer radius R_{out} and inner radius R_{in} by using the known transformation f_2 as shown in the complex form in Eq. (3.21). This mapping is shown in Figure 3.19.

$$\begin{aligned} Z_a &= R_a e^{i\Theta_a} \\ R_a(R_{cd}) &= R_{out} + \left(\frac{R_{out} - R_{in}}{R_{out}}\right) R_{cd} \\ \Theta_a &= \Theta_{cd} \end{aligned} \tag{3.21}$$

Here, R_{dc} and R_a are respectively the magnitude of Z_{cd} and Z_a, and Θ_{cd} and Θ_a are

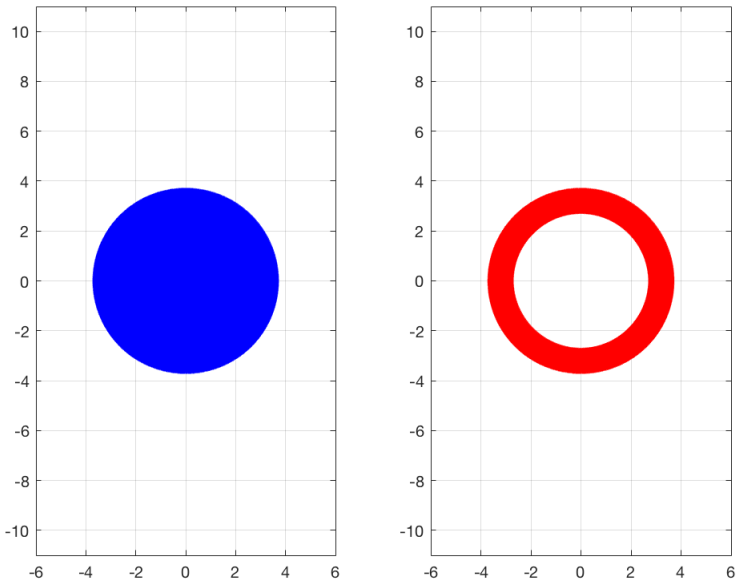

Figure 3.19: Mapping of circular disc centered at origin and of radius $R_c = 3.67$ to circular annulus of outer radius $R_{out} = 3.67$ and inner radius $R_{in} = \frac{3}{4}R_{out}$.

similarly the arguments of Z_{cd} and Z_a.

The annulus can now be mapped to a circle of radius $R_c = b$, as illustrated in Figure 3.20, by projecting its points on the unit circle and scaling the radius to R_c by using Eq. (3.22).

$$Z_c = R_c \frac{Z_a}{|Z_a|} \tag{3.22}$$

The circle of Figure 3.20 is centered at the origin and has a radius $R_c = b$. Thus, one can use the Karman-Trefftz transformation with parameter $\lambda = 2 - \frac{\alpha}{\pi}$ and b to map the aforementioned circle to a Karman-Trefftz airfoil of chord length $C = 2\lambda b$ and edge angles α. This is done by using Eq. (3.23) and is illustrated in Figure 3.21.

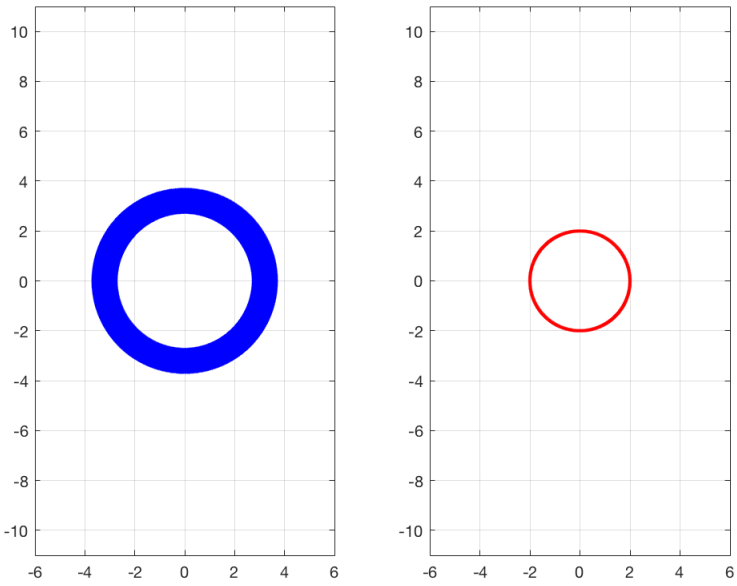

Figure 3.20: Mapping of circular annulus of outer radius $R_{out} = 3.67$ and inner radius $R_{in} = \frac{3}{4}R_{out}$ to circle of radius $R_c = 2$.

$$Z_{kt} = \lambda b \frac{(Z_c + b)^\lambda + (Z_c - b)^\lambda}{(Z_c + b)^\lambda - (Z_c - b)^\lambda} \tag{3.23}$$

Here, $b = R_c$ and $\lambda = 2 - \frac{\alpha}{\pi}$.

In the final step to determine transformation f that can be used to map a Karman-Trefftz disc to a Karman-Trefftz airfoil annulus as shown in Figure 3.15, one can re-scale the points Z_{kt} of the Karman-Trefftz airfoil profile to obtain the desired Karman-Trefftz airfoil annulus. This can be done by using Eq. (3.24) and is illustrated in Figure 3.22.

$$Z_{kta} = |Z_a| \frac{Z_{kt}}{\lambda R_c} \tag{3.24}$$

Here, $\lambda R_c = \lambda b = \frac{C}{2}$ is half the chord length C.

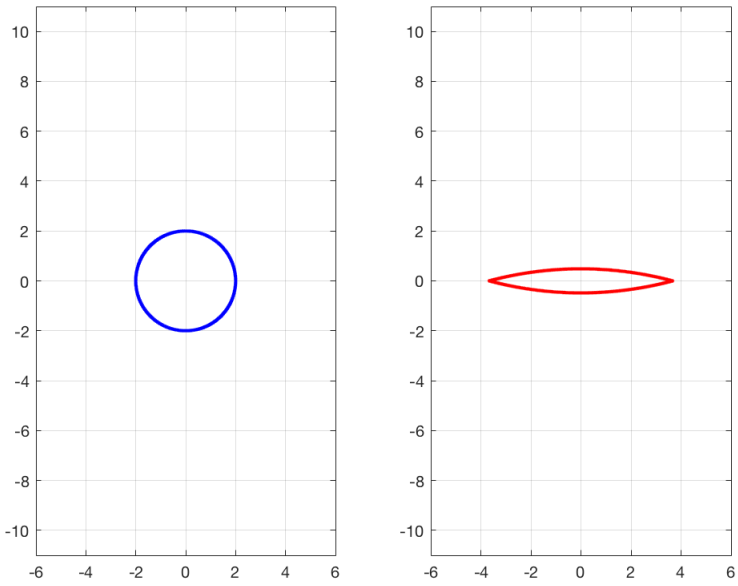

Figure 3.21: Mapping of circle of radius $R_c = 2$ to symmetric Karman-Trefftz airfoil profile of chord length $C = 7.33$ and edge angles $\alpha = \frac{\pi}{6}$.

The composition of the complex transformations of Eq. (3.18) - Eq. (3.24) can map a Karman-Trefftz airfoil disc to a Karman-Trefftz airfoil annulus and is illustrated in Figure 3.23. Unlike the approach with the Joukowski transformation, this sequence cannot be expressed explicitly in terms of the Cartersian or polar coordinates of the points on the initial Karman-Trefftz airfoil. This makes it more challenging, to determine the deformation gradient necessary for the formulation of cloaking devices by using the transformation approach. However, a numerical tool can be used to compute the necessary gradient. Moreover, the author found that the transformation changes the angular coordinates of initial points, the effect of those changes on a cloak formulation based on the transformation sequence has not been investigated. The author believes that this would have minimal effect and can be

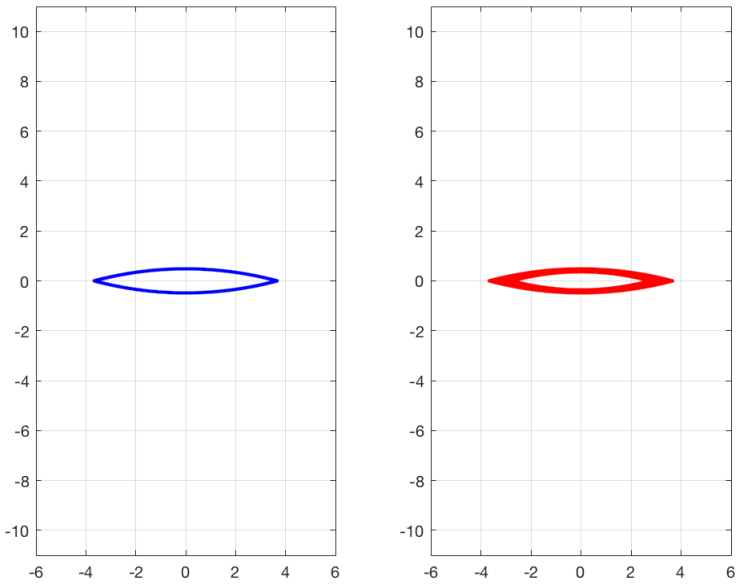

Figure 3.22: Mapping of symmetric Karman-Trefftz airfoil profile of chord length $C = 7.33$ and edge angles $\alpha = \frac{\pi}{6}$ to Karman-Trefftz airfoil annulus of outer chord length $C = 7.33$, inner chord length $c = \frac{3}{4}C$, and edge angles $\alpha = \frac{\pi}{6}$.

corrected through some angular transform if necessary; this remains to be explored.

3.4 Summary

The author has presented two efforts to find a sequence of transformations that can be used to formulate acoustic or electromagnetic airfoil cloaks by using the transformation method. The efforts are based on the Joukowski and the Karman-Trefftz transformation, two complex variable mappings that have been classically used to approximate airfoil geometries in aerodynamic studies. The effort based on the Joukowski transformation was only partially successful as one of the transformation in the sequence remains elusive. However, the shortcomings and approach of the ef-

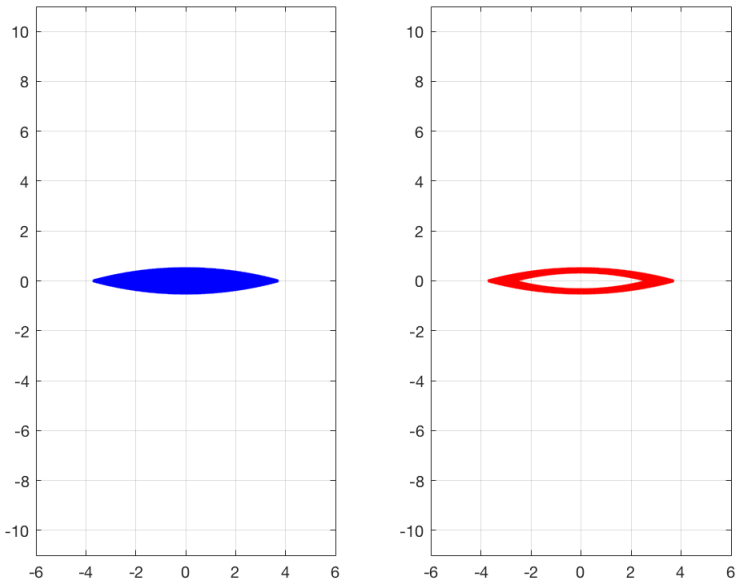

Figure 3.23: Mapping of symmetric Karman-Trefftz airfoil profile of chord length $C = 7.33$ and edge angles $\alpha = \frac{\pi}{6}$ to Karman-Trefftz airfoil annulus of outer chord length $C = 7.33$, inner chord length $c = \frac{3}{4}C$, and edge angles $\alpha = \frac{\pi}{6}$.

fort led to an alternative effort based on the Karman-Trefftz transformation. In this effort, the author took advantage of the mapping properties of the Karman-Trefftz transformation and leveraged the approach of the initial effort to successfully derive a sequence of transformation of a Karman-Trefftz airfoil disc to a Karman-Trefftz airfoil annulus. The investigation was only limited to symmetric Karman-Trefftz airfoils bounded by circular arc. The sequence can be used to formulate acoustic or electromagnetic cloaks for the aforementioned airfoils by using equations of the transformation approach to wave redirection. The sequence of transformation can be extended to more general Karman-Trefftz airfoils through astute mapping of those airfoils to the symmetric airfoils considered in the investigation. Also, it is

plausible that the approach based on the Joukowski transformation could be completed by successfully finding the incomplete transformation that maps a Joukowski airfoil disc to a circular disc. This transformation exists according to the Riemann mapping theorem. If successfully completed, the transformation sequence based on the Joukowski mapping can be very attractive for formulating airfoil cloaks using the transformation method. One of the main advantage of the Joukowski transformation is the simplicity of its expression. Thus, using the transformation could lead to explicit expressions and facilitate the calculations necessary for the formulation of cloaking devices. A hint of such simple explicit formulation was underscored in the foregoing discussion.

Chapter 4: Nonlinear Hyper-elastic Acoustic Metamaterial Studies

4.1 Overview

The derivation of the transformation method from the invariance of field equations often overshadows the fact that the approach is essentially a systematic formulation of refraction-based devices for controlling wave propagation path. Recall that in electromagnetics, the index of refraction n relates to the permitivity ϵ, and permeability μ as $n^2 \propto \epsilon\mu$, while in acoustics, the density ρ and bulk modulus κ of a material relate to the index of refraction through $n^2 \propto \rho/\kappa$. Consequently, Eq. (2.13) and Eq. (2.16) are mere formulations of refractive properties of an electromagnetic and acoustic wave redirection devices relative to their intended operational environment.

Unlike their electromagnetic counterparts, the refractive nature of acoustic wave redirection devices formulated through the transformation method restricts their design to metamaterials with fluid-like properties in which only longitudinal waves are allowed to propagate, and are readily controllable through refractive properties. Elastic solids, however, allow the propagation of both longitudinal and transverse waves because of their inherent ability to sustain both modes of defor-

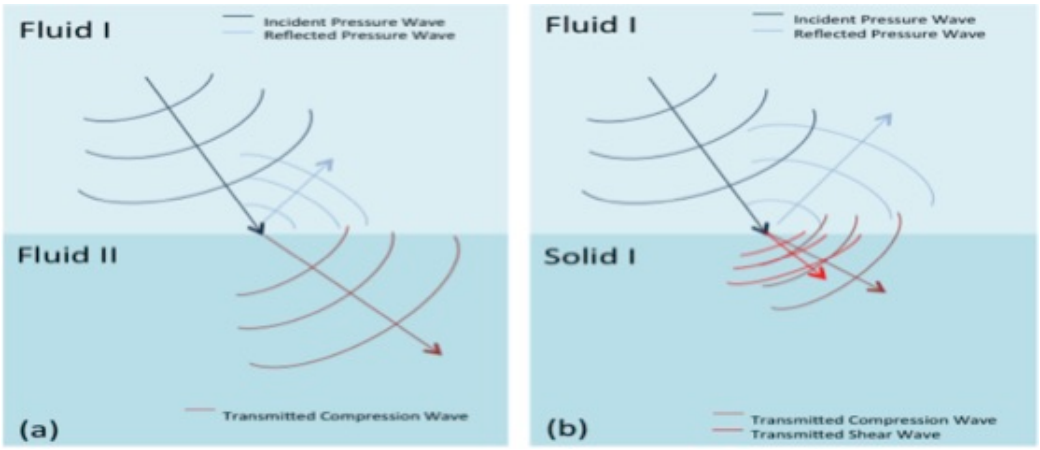

Figure 4.1: Acoustic wave refraction (a): fluid-fluid interface (b): fluid-solid interface.

mations [30]. Furthermore, in linear elastic materials, longitudinal and transverse waves refract differently because of differences in their phase speeds, and also propagate without interaction. This makes it challenging to simultaneously control their propagation paths through refractive properties alone.

$$c_l = \sqrt{\frac{\lambda + 2\mu}{\rho}} \text{ and } c_t = \sqrt{\frac{\mu}{\rho}} \tag{4.1}$$

Here, ρ represents density, and λ and μ are respectively the Lame's parameter and the shear modulus.

The propagation speeds of longitudinal and transverse waves in linear isotropic solids is given by Eq. (4.1), and it is observed that longitudinal waves propagate much faster than their transverse counterparts [30]. This results in two different indices of refraction for linear elastic solids, and a more complicated refractive behavior compared to fluids as illustrated in Figure 4.1.

In Figure 4.1(a), the familiar refraction scenario of a plane wave propagating from one fluid medium and incident upon the interface with another fluid medium is

shown. The transmitted wave through the second medium is refracted, but remains a single plane pressure wave. Thus, it is conceivable to use layers of fluid media with various refractive characterisitics to control the path of an acoustic wave as it propagates through the layers. However, in Figure 4.1(b) where the interfacing medium is an elastic solid, the phenomenon of mode conversion occurs as the propagating pressure wave from the fluid medium impinges on the fluid-solid boundary resulting in the transmission of a refracted longitudinal wave as well as a refracted transverse wave through the solid medium. This dual refractive characteristics of elastic solids makes their use challenging for controlling acoustic wave propagation through refraction.

To address the above mentioned quandary, an alternative solid material formulation based on pentamode materials was proposed by Norris in 2008 [31]. These peculiar solid materials were first introduced by Milton in 1997 and mimic fluid behavior in the limiting case. Their elasticity tensor has five near zero eigenvalues, hence the prefix "penta", which is associated with five compliant and one stiff modes [32]. Norris' work was a major breakthrough as it presented a pathway to potentially realize practical solid metamaterials for acoustic wave redirection [31]. However, in 2012, Kadic *et al.* built and tested a proposed pentamode design by Milton (see Figure 4.2), and revealed that the considered design presented practicability challenges due to an unfavorable trade-off between their desired pentamode behavior and their structural stability as observed in Figure 4.3[33]. In Figure 4.3, it is seen that the desired pentamode behavior degrades rapidly with increase structural stability; that is, the shear modulus increases much faster than the bulk modulus as

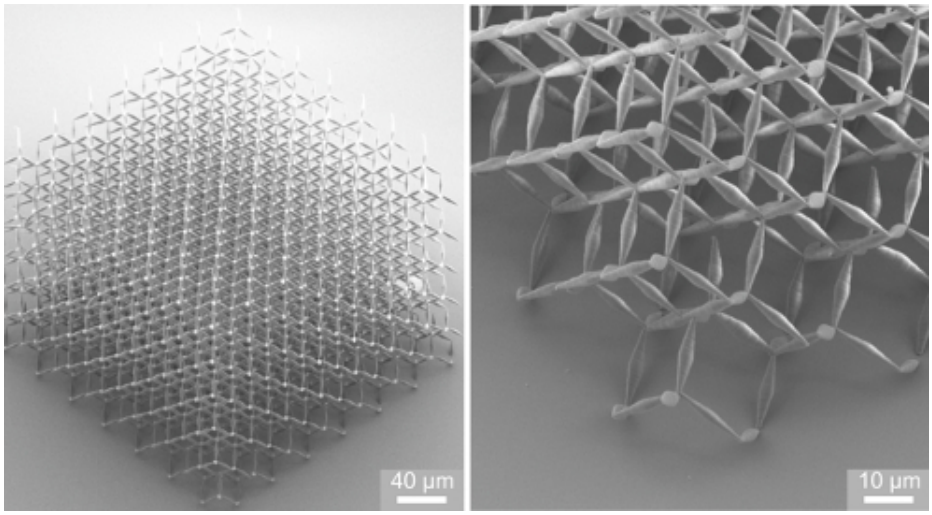

Figure 4.2: Proposed pentamode design by Milton. Sample polymer pentamode metamaterial cube fabricated using direct-laser-writing (DLW) [33].

the diameter of the connecting nodes increases. Nonetheless, despite the practical challenges that pentamodes may present, Norris' formulation remains at the forefront of acoustic metamaterials research today. Consequently, the emerging field of acoustic metamaterials remains open to novel approaches, which is the motivation for the investigation set forth in this chapter.

Before proceeding, it needs to be underscored that the previous discussion pertains solely to wave redirection mechanisms on the basis of linear system behavior. The refraction scenario depicted in Figure 4.1(b) is applicable only to linear elastic solids wherein the refracted longitudinal and transverse waves are transmitted through the solid medium without interaction as stipulated by the principle of superposition. A richer and more complex wave behavior can manifest if nonlinearity is allowed in the solid medium. Unlike their linear counterparts, nonlinear waves seldom propagate without interaction, and these waves are amenable to combina-

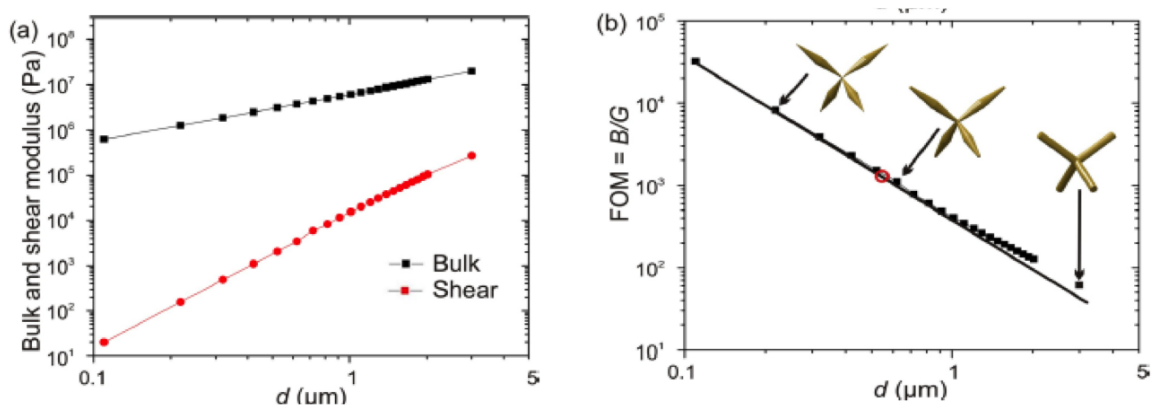

Figure 4.3: Structural stability trade-off study for pentamode design [33].

tions and new wave formations that lead to a plethora of phenomena exploitable for practical applications [34, 35]. In this chapter, the author summarizes an effort to exploits nonlinearities (geometric and material), and nonlinear wave phenomena to formulate a hyper-elastic acoustic metamaterial favorable to the control of acoustic wave propagation path. The formulated material model is investigated for plane wave propagation by using perturbation and approximation analyses available for studies of nonlinear waves.

4.2 Theory

4.2.1 Murnaghan strain energy function in elastoacoustic studies

Elastoacoustic investigations are classically formulated from the nonlinear hyper-elastic material model first proposed by Murnaghan in 1937 [36]. In its classical form, the Murnaghan model is a third order strain energy density function of components of Green-Lagrange strain tensor, and is shown in Eq. (4.2) [36, 37]. The model can

be used to describe the behavior of a large class of engineering materials, including many metals, when material nonlinearity is accounted for [37].

$$W(\epsilon_{ij}) = \frac{1}{2}\lambda(\epsilon_{mm})^2 + \mu(\epsilon_{ik})^2 + \frac{1}{3}A\epsilon_{ik}\epsilon_{im}\epsilon_{km} + B(\epsilon_{ik})^2\epsilon_{mm} + \frac{1}{3}C(\epsilon_{mm})^3 \qquad (4.2)$$

Here, the second order constants λ and μ are commonly referred to as Lame's elastic constants, and the constants of the third order A, B, and C are the Murnaghan material constants [37].

For wave propagation problems, it is convenient and common practice to re-express the model given by Eq. (4.2) in terms of gradients of the displacements u_k by using the relationship between Green-Lagrange strain tensor and the displacement gradients tensor Eq. (4.3) [37].

$$\epsilon_{nm} = \frac{1}{2}(u_{n,m} + u_{m,n} + u_{k,n}u_{k,m}) \qquad (4.3)$$

Here, $\mathbf{u}(\mathbf{x_k}, \mathbf{t})$ is the displacement vector.

The resulting formulation is shown in Eq. (4.4), and is more suited for the types of initial and boundary conditions ordinarily encountered in wave propagation problems.

$$
\begin{aligned}
W(u_{i,k}) = {} & \frac{1}{2}\lambda(u_{m,m})^2 + \frac{1}{4}\mu(u_{i,k}+u_{k,i})^2 + (\mu + \frac{1}{4}A)u_{i,k}u_{m,ki}u_{m,k} \\
& + \frac{1}{2}(\lambda+B)u_{m,m}(u_{i,k})^2 + \frac{1}{12}Au_{i,k}u_{k,m}u_{m,i} + \frac{1}{2}Bu_{i,k}u_{k,i}u_{m,m} + \frac{1}{3}C(u_{m,m})^3 \\
& + \frac{1}{4}\lambda(U_{n,m})^3 + \frac{1}{4}\mu(u_{n,i}u_{n,k})^2 + \frac{1}{8}A[(u_{i,k}+u_{k,i})(u_{i,m}+u_{m,i})u_{s,k}u_{s,m} \\
& + (u_{i,k}+u_{k,i})(u_{k,m},u_{m,k})u_{s,i}u_{s,m} + (u_{i,m}+u_{m,i})(u_{k,m}+u_{m,k})u_{s,i}u_{s,k} \\
& + \frac{1}{2}B[(u_{i,k}+u_{k,i})u_{n,i}u_{n,k}u_{m,m} + \frac{1}{2}(u_{i,k}u_{k,i}+u_{i,k}u_{i,k})u_{n,m}u_{n,m}] \\
& + \frac{3}{2}C(u_{m,m})^2(u_{n,m})^2 + \frac{1}{24}A[(u_{i,k}+u_{k,i})(u_{s,i}u_{s,m})(u_{l,k}u_{l,m}) \\
& + (u_{i,m}+u_{m,i})(u_{n,i}u_{n,k})(u_{l,k}u_{l,m}) + (u_{k,m}+u_{m,k})(u_{n,i}u_{n,k})(u_{s,i}u_{s,k})] \\
& + \frac{1}{4}B[(u_{n,i}u_{n,k})^2u_{m,m} + (u_{i,k}+u_{k,i})u_{n,i}u_{n,k}(u_{s,m})^2] + \frac{1}{12}Cu_{m,m}(u_{n,m})^4 \\
& + \frac{1}{24}A(u_{n,i}u_{n,k})(u_{s,i}u_{s,m})(u_{l,k}u_{l,m}) + \frac{1}{8}B(u_{n,i}u_{n,k})^2(u_{s,m})^2 + \frac{1}{24}C(u_{n,m})^6
\end{aligned}
\tag{4.4}
$$

It should be noted that the strain energy function of Eq. (4.4) encompasses both material and geometric nonlinearities as no assumption of infinitesimal displacement is made in Eq. (4.3). And, unlike Eq. (4.2), which includes only third powers of the strain components, Eq. (4.4) now includes up to sixth powers of the displacement gradients. This allows for four nonlinear sub-potentials to be considered in the study of wave propagation problems. The simplest sub-potential, Eq. (4.5), is obtained by neglecting terms of the fourth through six powers of the displacement gradients. This was used in seminal papers on plane nonlinear elastic waves in elastoacoustics studies [37, 38].

$$W(u_{i,k}) = \frac{1}{2}\lambda(u_{m,m})^2 + \frac{1}{4}\mu(u_{i,k}+u_{k,i})^2 + (\mu + \frac{1}{4}A)u_{i,k}u_{m,ki}u_{m,k} + \frac{1}{2}(\lambda+B)u_{m,m}(u_{i,k})^2 + \frac{1}{12}Au_{i,k}u_{k,m}u_{m,i} + \frac{1}{2}Bu_{i,k}u_{k,m}u_{m,m} + \frac{1}{3}C(u_{m,m})^3 \tag{4.5}$$

4.2.2 Plane waves in classical nonlinear Murnaghan materials

The third order sub-potential of Eq. (4.5) can be further simplified for plane polarized wave propagation problems where the wave front is assumed to be dependent on only one coordinate variable; that is, x_1, x_2, or x_3. The resulting sub-potential is shown in Eq. (4.6) for the case of a wave vector directed along the abcissa x_1 [37, 38].

$$W = \frac{1}{2}[(\lambda+2\mu)(u_{1,1})^2 + \mu[(u_{2,1})^2 + (u_{3,1})^2]] + [\mu + \frac{1}{2}\lambda + \frac{1}{3}A + B + \frac{1}{3}C](u_{1,1})^3 + [\frac{1}{2}(\lambda+B) + (\mu+\frac{1}{4}A)]u_{1,1}[(u_{2,1})^2 + (u_{3,1})^2] \tag{4.6}$$

Recalling that the components of the First Piola-Kirchoff stress tensor t_{ik} relates to the strain energy function as $t_{ik} = \partial W/\partial u_{i,j}$, the three stress expressions of Eq. (4.7) are derived for the propagation of plane waves in the simplest Murnaghan materials.

$$
\begin{aligned}
t_{11} &= (\lambda + 2\mu)u_{1,1} + \frac{3}{2}[\lambda + 2\mu + 2(\frac{A}{3} + B + \frac{C}{3})](u_{1,1})^2 \\
&\quad + \frac{1}{2}[\lambda + 2\mu + \frac{1}{2}A + B][(u_{2,1})^2 + (u_{3,1})^2], \\
t_{12} &= \mu u_{2,1} + \frac{1}{2}[\lambda + 2\mu + \frac{1}{2}A + B]u_{1,1}u_{2,1}, \\
t_{13} &= \mu u_{3,1} + \frac{1}{2}[\lambda + 2\mu + \frac{1}{2}A + B]u_{1,1}u_{3,1}
\end{aligned}
\tag{4.7}
$$

After substituting the stress components into Euler's mass balance equation $\rho\ddot{u_k} = t_{ik,i} + F_k$, the result is the three coupled nonlinear wave equations of Eq. (4.8), which govern the propagation of plane waves in the simplest Murnaghan's hyper-elastic materials of Eq. (4.6)[38, 39].

$$
\begin{aligned}
\rho u_{1,tt} - (\lambda + 2\mu)u_{1,11} &= N_1 u_{1,11}u_{1,1} + N_2(u_{2,11}u_{2,1} + u_{3,11}u_{3,1}), \\
\rho u_{2,tt} - \mu u_{2,11} &= N_2(u_{2,11}u_{1,1} + u_{1,11}u_{2,1}), \\
\rho u_{3,tt} - \mu u_{3,11} &= N_2(u_{3,11}u_{1,1} + u_{1,11}u_{3,1})
\end{aligned}
\tag{4.8}
$$

Here, $N_1 = 3[(\lambda + 2\mu) + 2(\frac{A}{3} + B + \frac{C}{3})], N_2 = \lambda + 2\mu + \frac{1}{2}A + B$

Although nonlinear and inhomogenous, note that Eq. (4.8) was arranged in a simple and intuitive form by regrouping all nonlinear terms to the right hand side (RHS) of the equation whilst keeping the linear terms on the left hand side (LHS). In this form, known as Lame's form, the LHS terms are classical linear wave equations, while the RHS terms can be viewed as nonlinear source terms and provide an insight into the problem of interest[37, 40]. Indeed, the form of Eq. (4.8) reveals an inherent feature of the system, a coupling between the longitudinal and transverse equations, which is evident from the RHS terms of the first equation of Eq. (4.8); that is, the equation governing the longitudinal response of the material.

From these terms it can be inferred that a purely transverse excitation can result in a longitudinal response in the material even in the absence of a longitudinal excitation [37, 38]. However, the aforementioned coupling phenomenon is not bi-directional as the equations governing the transverse responses, the last two equations of Eq. (4.8), show that a purely longitudinal excitation would not conversely result in a transverse response of the material. This can be made more evident by exploring the solutions of Eq. (4.8) for plane longitudinal and transverse wave excitations at the boundary.

In exploring plane wave propagation in Murnaghan materials defined by the strain energy function of Eq. (4.6), the system of nonlinear wave equations of Eq. (4.8) must be solved for zero initial conditions, and prescribed boundary conditions of the form $u_i(0,t) = U_i cos(\omega t)$, where U_i is the amplitude of the harmonic excitation at the boundary. The system lends itself to a number of classical solution methods of nonlinear analysis such as the Method of Successive Approximations [37], or the Straightforward Perturbation Method [41]. The former has classically been the method of choice for elastoacoustics problems because of its relative simplicity, and was used by Cattani and Ruschitsky to investigate quadradically nonlinear plane wave propagation in Murnaghan materials [38]. Through successive approximations up to the second approximation, Cattani and Rushchitsky demonstrated that the solutions to Eq. (4.8) when subjected respectively to the set of boundary conditions shown in Eq. (4.9) and Eq. (4.10), are given by Eq. (4.11), and Eq. (4.12). These correspond respectively to the plane wave response of nonlinear Murnaghan materials of Eq. (4.6) to longitudinal, and transverse harmonic boundary excitation [37, 38].

$$u_1(0,t) = U_1 cos(\omega t)$$
$$u_2(0,t) = u_3(0,t) = 0 \tag{4.9}$$

$$u_1(0,t) = u_2(0,t) = 0$$
$$u_3(0,t) = U_3 cos(\omega t) \tag{4.10}$$

$$u_1(x,t) = U_1 cos(k_L x_1 - \omega t) + x_1 \frac{N_1}{8(\lambda + 2\mu)} U_1^2 k_L^2 cos2(k_L x_1 - \omega t) \tag{4.11}$$

Here, $k_L = \frac{\omega}{v_L}$ is the longitudinal wave number.

$$u_1(x,t) = \frac{\lambda + 2\mu + \frac{1}{2}A + B}{4\rho(v_L^2 + v_T^2)} k_3 U_3^2 sin((k_3 - k_1)x_1) cos(2\omega t - (k_3 - k_1)x_1),$$
$$u_3(x,t) = U_3 cos(\omega t - k_3 x_1) \tag{4.12}$$

From Eq. (4.11) and Eq. (4.12), it is noted that unlike the response to longitudinal harmonic excitation at the boundary, which results in the propagation of only longitudinal waves, the response to transverse excitation of the material is rather bi-modal [37, 38]. Indeed, consistent with the earlier observation, by using Eq. (4.12) one can prove that a transverse boundary excitation in Murnaghan materials of Eq. (4.6) results inherently in both transverse and longitudinal responses even in the absence of a longitudinal excitation.

4.3 Acoustic metamaterial formulation with nonlinear coupling

The above results from Cattani and Rutschistky demonstrate that nonlinear Murnaghan materials of Eq. (4.6) are inherently amenable to transfer of energy be-

tween longitudinal and transverse modes during plane wave propagation as a result of the intrinsic coupling between the two modes. However, the energy transfer is uni-directional from transverse to longitudinal mode; that is, a transverse excitation yields both a transverse response and a longitudinal response in the material, whereas a longitudinal excitation results solely in a longitudinal response. Though potentially exploitable for other applications, this inherent coupling phenomenon remains unfavorable to refraction-based acoustic wave redirection. Recall from Eq. (4.1) and Section 4.1 that in elastic solid media, longitudinal waves propagate significantly faster than transverse waves. Thus, to achieve a refractive behavior conducive to acoustic wave redirection by using elastic solids, it is rather the converse transfer of wave energy from longitudinal to transverse mode that needs to be sought. Here, the question naturally arises, based on the foregoing treatment, of whether such transfer of energy is theoretically achievable through suitable modifications of the Murnaghan strain energy function of Eq. (4.6). In the remainder of this chapter, the author's effort to answer that question and to formulate a hyper-elastic material amenable to the transfer of energy from longitudinal to transverse mode during plane wave propagation is described. Such materials, if physically realizable through metamaterial technology, are postulated to exhibit a more suitable refractive behavior for controlling acoustic wave propagation paths.

4.3.1 Modification to the Murnaghan strain energy function

Typically, strain energy functions, including that of Eq. (4.6), can be used to model the behavior of a material or class of physical materials for which experimental data can be obtained to assess the validity of the formulated model as well as its limitations. Often, the model is obtained by solving an inverse problem where observable behaviors of the material or material class of interest are the basis for the mathematical properties and parameters required for the model. Once a model is developed, a well-posed forward problem with defined loading, initial, and boundary conditions, are solved to evaluate and validate the formulated model [42]. The author adopted a similar inverse problem approach in exploring necessary modifications to the the Murnaghan strain energy function of Eq. (4.6) to achieve the sought-after energy transfer. However, in this case, the aim of the formulation is not to model the behavior of a physical material, but rather that of a hypothetical hyper-elastic metamaterial with the desired mode coupling behavior underscored earlier.

Starting first from Eq. (4.7) and Eq. (4.8), it is recognized that the last term, $\frac{1}{2}[\lambda + 2\mu + \frac{1}{2}A + B][(u_{2,1})^2 + (u_{3,1})^2]$, of the longitudinal stress equation of Eq. (4.7) engenders the coupling of the longitudinal and transverse wave equations in Eq. (4.8), which results in the demonstrated inherent coupling of the two modes of wave propagation in Murnaghan materials defined by Eq. (4.6). Through mathematical integration, it is not a tedious task to relate the aforementioned coupling term in the longitudinal stress equation to the last term, $(\mu + \frac{1}{4}A)]u_{1,1}[(u_{2,1})^2 + (u_{3,1})^2]$, of the

strain energy function Eq. (4.6). This provide an intuitive insight into modifications to Eq. (4.6) necessary to achieve the sought-after energy transfer from longitudinal to transverse mode during plane wave propagation. The above observations suggests that a coupling term of the form $\alpha u_{1,1}^2(u_{2,1} + u_{3,1})$ be added to Eq. (4.6). The resulting modified strain energy function is shown in Eq. (4.13), where the coupling parameter α is an additional third order material constant similar to A, B, and C. As with classical inverse problems, the formulated material of Eq. (4.13) must be investigated to assess the validity of the hypothesis that led to this formulation. To that end, it is required to derive the governing wave equations as in Section 4.2.1 in order to set and solve the forward problem of a prescribed harmonic longitudinal and transverse plane wave excitation at the boundary.

$$\begin{aligned} W(u_{i,k}) = \frac{1}{2}[(\lambda + 2\mu)(u_{1,1})^2 + \mu[(u_{2,1})^2 + (u_{3,1})^2]] + [\mu + \frac{1}{2}\lambda + \frac{1}{3}A + B + \frac{1}{3}C](u_{1,1})^3 \\ + [\frac{1}{2}(\lambda + B) + (\mu + \frac{1}{4}A)]u_{1,1}[(u_{2,1})^2 + (u_{3,1})^2] + \alpha u_{1,1}^2(u_{2,1} + u_{3,1}) \end{aligned} \tag{4.13}$$

Proceeding as in Section 4.2.1, the components of the First Piola-Kirchoff stress associated with the modified strain energy function are derived from $t_{ik} = \partial W/\partial u_{i,j}$, and shown in Eq. (4.14).

$$\begin{aligned} t_{11} &= (\lambda + 2\mu)u_{1,1} + (\frac{3}{2}[\lambda + 2\mu + 2(\frac{A}{3} + B + \frac{C}{3})](u_{1,1})^2 \\ &\quad + \frac{1}{2}[\lambda + 2\mu + \frac{1}{2}A + B][(u_{2,1})^2 + (u_{3,1})^2] + 2\alpha u_{1,1}(u_{2,1} + u_{3,1}), \\ t_{12} &= \mu u_{2,1} + \frac{1}{2}[\lambda + 2\mu + \frac{1}{2}A + B]u_{1,1}u_{2,1} + \alpha(u_{1,1})^2, \\ t_{13} &= \mu u_{3,1} + \frac{1}{2}[\lambda + 2\mu + \frac{1}{2}A + B]u_{1,1}u_{3,1} + \alpha(u_{1,1})^2 \end{aligned} \tag{4.14}$$

The three nonlinear wave equations ensuing from the above stresses are found as before from Euler's balance equation $\rho\ddot{u_k} = t_{ik,i} + F_k$ and shown in Eq. (4.15).

$$\begin{aligned}
\rho u_{1,tt} - (\lambda + 2\mu)u_{1,11} &= N_1 u_{1,11}u_{1,1} + N_2(u_{2,11}u_{2,1} + u_{3,11}u_{3,1}) \\
&\quad + N_3[u_{1,1}(u_{2,11} + u_{3,11}) + u_{1,11}(u_{2,1} + u_{3,1})], \\
\rho u_{2,tt} - \mu u_{2,11} &= N_2(u_{2,11}u_{1,1} + u_{1,11}u_{2,1}) + N_3 u_{1,1}u_{1,11}, \\
\rho u_{3,tt} - \mu u_{3,11} &= N_2(u_{3,11}u_{1,1} + u_{1,11}u_{3,1}) + N_3 u_{1,1}u_{1,11}
\end{aligned} \tag{4.15}$$

Here, $N_1 = 3[(\lambda + 2\mu) + 2(\frac{A}{3} + B + \frac{C}{3})], N_2 = \lambda + 2\mu + \frac{1}{2}A + B, and N_3 = 2\alpha$.

Through simple observation of the RHS terms of the last two equations of Eq. (4.15), it can be noted that a longitudinal disturbance, even in the absence of any transverse counterpart, would induce a transverse response of the material as a direct sequel of the introduced coupling parameter α. Also note that in the modified model, the inherent coupling of Murnaghan strain energy function is maintained. To further explore the behavior of the formulated material, the nonlinear wave equations of Eq. (4.15) are next solved for longitudinal and transverse harmonic excitations at the boundary.

4.3.2 Response to longitudinal harmonic excitation at the boundary

As mentioned in Section 4.2.1, a number of analytical tools are available to solve nonlinear wave equations of the form of Eq. (4.15). This includes the Method of Successive Approximations, which has classically been the method of choice in elastoacoustics studies as was used by Cattani and Rutchisky in their various inves-

tigations of wave propagation in hyperelastic materials [38, 43]. However, for a more rigorous mathematical treatment of Eq. (4.15), the broadly applicable Straightforward perturbation analysis is used to explore plane wave propagation in materials governed by Eq. (4.13). The use of this perturbation analysis facilitates in understanding how the strengths of the different nonlinear terms influence the response. To that end, the case of a harmonic longitudinal plane wave (P-wave) prescribed at the boundary of a semi-infinite half space $0 \leq x_1 < \infty$ is first considered. This is equivalent to solving Eq. (4.15) for the following set of initial and boundary conditions.

$$\begin{aligned}
&u_1(x_1,0) = u_{1,t}(x_1,0) = 0,\ 0 \leq x_1 < \infty \qquad u_1(0,t) = U_1 cos(\omega t),\ t > 0 \\
&u_2(x_1,0) = u_{2,t}(x_1,0) = 0,\ 0 \leq x_1 < \infty \qquad u_2(0,t) = 0,\ t > 0 \\
&u_3(x_1,0) = u_{3,t}(x_1,0) = 0,\ 0 \leq x_1 < \infty \qquad u_3(0,t) = 0,\ t > 0
\end{aligned} \tag{4.16}$$

Since a perturbation solution is sought, a small amplitude is assumed for the displacement, a valid assumption for elastoacoustic problems. Thus, the boundary conditions can be rewritten as in Eq.4.17 below.

$$\begin{aligned}
&u_1(0,t) = \epsilon U_1 cos(\omega t).\ \text{ for } t > 0 \\
&u_2(0,t) = 0 \\
&u_2(0,t) = 0
\end{aligned} \tag{4.17}$$

Here, ϵ is a small nondimensional scaling parameter that is a measure of the amplitude of the displacement and used here as a bookkeeping parameter for the perturbation analysis. The above assumption suggests an expansion of the solutions to Eq. (4.15) is sought in the following form:

$$
\begin{aligned}
u_1(x_1,t,\epsilon) &= \epsilon u_1^{(1)}(x_1,t) + \epsilon^2 u_1^{(2)}(x_1,t) + \epsilon^3 u_1^{(3)}(x_1,t) + ... + \epsilon^n u_1^{(n)}(x_1,t) \\
u_2(x_1,t,\epsilon) &= \epsilon u_2^{(1)}(x_1,t) + \epsilon^2 u_2^{(2)}(x_1,t) + \epsilon^3 u_2^{(3)}(x_1,t) + ... + \epsilon^n u_2^{(n)}(x_1,t) \\
u_3(x_1,t,\epsilon) &= \epsilon u_3^{(1)}(x_1,t) + \epsilon^2 u_3^{(2)}(x_1,t) + \epsilon^3 u_3^{(3)}(x_1,t) + ... + \epsilon^n u_3^{(n)}(x_1,t)
\end{aligned} \tag{4.18}
$$

where $\epsilon u_i^{(1)}(x_1,t)$ is referred to as the first-order term in the expansion, $\epsilon^2 u_i^{(2)}(x_1,t)$, as the second-order term, $\epsilon^3 u_i^{(3)}(x_1,t)$,as the third-order term, and so on up to the nth-order term $\epsilon^n u_i^{(n)}(x_1,t)$ [41].

Before proceeding with the perturbation analysis, the above expansion for the solution must first be substituted into the boundary conditions as shown in Eq. (4.19).

$$
\begin{aligned}
&\epsilon u_1^{(1)}(0,t) + \epsilon^2 u_1^{(2)}(0,t) + \epsilon^3 u_1^{(3)}(0,t) + ... + \epsilon^n u_1^{(n)}(0,t) = U_1 cos(\omega t) \\
&\epsilon u_2^{(1)}(0,t) + \epsilon^2 u_2^{(2)}(0,t) + \epsilon^3 u_2^{(3)}(0,t) + ... + \epsilon^n u_2^{(n)}(0,t) = 0 \\
&\epsilon u_3^{(1)}(0,t) + \epsilon^2 u_3^{(2)}(0,t) + \epsilon^3 u_3^{(3)}(0,t) + ... + \epsilon^n u_3^{(n)}(0,t) = 0
\end{aligned} \tag{4.19}
$$

From Eq. (4.19), the appropriate set initial and boundary conditions are obtained and shown in Eq. (4.20).

$$
\begin{aligned}
u_1^{(1)}(x_1,0) &= 0 \qquad u_1^{(1)}(0,t) = U_1 cos(\omega t) \\
&\qquad\quad u_1^{(n)}(0,t) = 0 \\
u_2^{(n)}(x_1,0) &= 0 \qquad u_2^{(n)}(0,t) = 0 \\
u_3^{(n)}(x_1,0) &= 0 \qquad u_2^{(n)}(0,t) = 0
\end{aligned} \tag{4.20}
$$

The author now proceeds with the solution steps by first substituting the assumed expansion of Eq. (4.18) into the three wave equations of Eq. (4.15) and

collecting terms of like powers of ϵ. Starting with order ϵ, one obtains the set of homogeneous linear wave equations shown in Eq. (4.21), and corresponding boundary conditions. Note that initial conditions, as in representation Eq. (4.21), would not be explicitly stated unless they have non-zero values.

Order (ϵ):

$$\begin{aligned} u^{(1)}_{1,tt} - c_1^2 u^{(1)}_{1,11} = 0, \text{ with } u^{(1)}_1(0,t) = U_1 cos(\omega t) \\ u^{(1)}_{2,tt} - c_2^2 u^{(1)}_{2,11} = 0, \text{ with } u^{(1)}_2(0,t) = 0 \\ u^{(1)}_{3,tt} - c_3^2 u^{(1)}_{3,11} = 0, \text{ with } u^{(1)}_3(0,t) = 0 \end{aligned} \tag{4.21}$$

Here, $c_1 = \sqrt{\frac{\lambda+2\mu}{\rho}}$ is the linear longitudinal phase speed, and $c_2 = c_3 = \sqrt{\frac{\mu}{\rho}}$ are the transverse linear phase speeds.

Given zero initial conditions, the first two equations of Eq. (4.21) have the trivial solutions of shown in Eq. (4.22)

$$u^{(1)}_2(x_1,t) = 0 u^{(1)}_3(x_1,t) \quad = 0 \tag{4.22}$$

And, Eq. (4.23), the solution to the first equation, can readily be found in any classical partial differential equations text book or simply by using D'Alembert formula.

$$u^{(1)}_1(x_1,t) = U_1 \cos(k_1 x_1 - \omega t) \tag{4.23}$$

Here, the wave number $k_1 = \frac{\omega}{c_1}$.

With the solution at order ϵ found, the author proceeds with collection of terms of order ϵ^2. The resulting linear wave equations, Eq. (4.24), are in-homogeneous,

but with homogeneous boundary conditions.

Order (ϵ^2):

$$\begin{aligned} u^{(2)}_{1,tt} - c_1^2 u^{(2)}_{1,11} &= \frac{N_1}{\rho} u^{(1)}_{1,1} u^{(1)}_{1,11}, \text{ with } u^{(2)}_1(0,t) = 0 \\ u^{(2)}_{2,tt} - c_2^2 u^{(2)}_{2,11} &= \frac{N_3}{\rho} u^{(1)}_{1,1} u^{(1)}_{1,11}, \text{ with } u^{(2)}_2(0,t) = 0 \\ u^{(2)}_{3,tt} - c_3^2 u^{(2)}_{3,11} &= \frac{N_3}{\rho} u^{(1)}_{1,1} u^{(1)}_{1,11}, \text{ with } u^{(2)}_3(0,t) = 0 \end{aligned} \tag{4.24}$$

Note that the in-homogeneous part of the wave equations at order ϵ^2, there is dependence solely on the known solution $u^{(1)}_1(x_1,t)$ at order ϵ. This is a hallmark of perturbation methods where the substitution of the assumed solutions lead to equations of subsequent orders of the perturbation parameter that are dependent on the solutions of equations at previous orders allowing the problem to be solved sequentially [41]. On substituting $u^{(1)}_1(x_1,t)$ into Eq. (4.24) the result is:

Order (ϵ^2):

$$\begin{aligned} u^{(2)}_{1,tt} - c_1^2 u^{(2)}_{1,11} &= \frac{N_1}{\rho} U_1^2 k_1^3 \sin(k_1 x_1 - \omega t)\cos(k_1 x_1 - \omega t), \text{ with } u^{(2)}_1(0,t) = 0 \\ u^{(2)}_{2,tt} - c_2^2 u^{(2)}_{2,11} &= \frac{N_3}{\rho} U_1^2 k_1^3 \sin(k_1 x_1 - \omega t)\cos(k_1 x_1 - \omega t), \text{ with } u^{(2)}_2(0,t) = 0 \\ u^{(2)}_{3,tt} - c_3^2 u^{(2)}_{3,11} &= \frac{N_3}{\rho} U_1^2 k_1^3 \sin(k_1 x_1 - \omega t)\cos(k_1 x_1 - \omega t), \text{ with } u^{(2)}_3(0,t) = 0 \end{aligned} \tag{4.25}$$

The in-homogeneous wave equations of Eq. (4.25) can be solved by using Duhamel's Principle [40] by considering the nonlinear RHS term as a source term. Duhamel's Principle allows the solutions of a linear in-homogeneous partial differential equation (PDE) with zero initial conditions, by moving the source term to the initial conditions as an initial velocity, and solving the ensuing homogeneous problem [40]. Applying this methodology, the solution to Eq. (4.25) is found to be:

$$
\begin{aligned}
u_1^{(2)}(x_1,t) &= \frac{N_1}{8(\lambda+2\mu)} U_1^2 k_1^2 x_1 \cos[2(k_1 x_1 - \omega t)] \\
u_2^{(2)}(x_1,t) &= \frac{N_2}{4\rho(c_2^2-c_1^2)} U_1^2 k_1 \sin[(k_1-k_2)x_1] \cos[(k_1+k_2)x_1 - 2\omega t)] \\
u_3^{(2)}(x_1,t) &= \frac{N_2}{4\rho(c_3^2-c_1^2)} U_1^2 k_1 \sin[(k_1-k_3)x_1] \cos[(k_1+k_3)x_1 - 2\omega t)]
\end{aligned}
\tag{4.26}
$$

Here, the wave number $k_i = \frac{\omega}{c_i}$.

With the solutions at order ϵ and ϵ^2 determined, the next solution step is to collect terms of order ϵ^3, which would lead to much more complex set of equations. However, undertaking such a daunting task is deemed inessential to the objective of the effort. Furthermore, the solutions at order ϵ^3 and beyond are not expected to be of significant contribution to the overall response when ϵ is assumed to be small.

By substituting Eq. (4.23) and Eq. (4.26) into the assumed solution expansion of Eq. (4.18), the expansion solution to Eq. (4.15) up to order ϵ^2 is constructed and shown in Eq. (4.27). This is the response of a semi-infinite space of materials governed by the modified Murnaghan strain energy model of Eq. (4.13) to longitudinal harmonic excitation prescribed at the boundary.

$$
\begin{aligned}
u_1(x_1,t,\epsilon) &= \epsilon U_1 \cos(k_1 x_1 - \omega t) + \epsilon^2 \frac{N_1}{8(\lambda+2\mu)} U_1^2 k_1^2 x_1 \cos[2(k_1 x_1 - \omega t)] \\
u_2(x_1,t,\epsilon) &= \epsilon^2 \frac{N_3}{4\rho(c_2^2-c_1^2)} U_1^2 k_1 \sin[(k_1-k_2)x_1] \cos[(k_1+k_2)x_1 - 2\omega t)] \\
u_3(x_1,t,\epsilon) &= \epsilon^2 \frac{N_3}{4\rho(c_3^2-c_1^2)} U_1^2 k_1 \sin[(k_1-k_3)x_1] \cos[(k_1+k_3)x_1 - 2\omega t)]
\end{aligned}
\tag{4.27}
$$

Before proceeding with the analysis of Eq. (4.27), it can be noted that both the longitudinal u_1, and transverse solutions u_2 and u_3 in Eq. (4.15) are dependent on the amplitude U_1 of the harmonic excitation and the scaling constant ϵ that also

served as perturbation parameter. The observed dependence is in the form of ϵU_1, which allows the scaling constant ϵ to be absorbed by setting $\epsilon = 1$, and alternatively considering U_1 as the perturbation parameter with $|U_1| << 1$. Consequently, solution shown in Eq. (4.27) can be rewritten without ϵ in terms of only the excitation amplitude U_1 as in Eq. (4.28) below.

$$
\begin{aligned}
u_1(x_1,t) &= U_1\cos(k_1x_1-\omega t) + \frac{N_1}{8(\lambda+2\mu)}U_1^2k_1^2x_1\cos[2(k_1x_1-\omega t)] \\
u_2(x_1,t) &= \frac{N_3}{4\rho(c_2^2-c_1^2)}U_1^2k_1\sin[(k_1-k_2)x_1]\cos[(k_1+k_2)x_1-2\omega t)] \\
u_3(x_1,t) &= \frac{N_3}{4\rho(c_3^2-c_1^2)}U_1^2k_1\sin[(k_1-k_3)x_1]\cos[(k_1+k_3)x_1-2\omega t)]
\end{aligned}
\tag{4.28}
$$

Contrasting Eq. (4.28) with Eq. (4.11) one can see that the longitudinal response of the formulated material to longitudinal plane wave excitation, Eq. (4.13), is similar to that of a Murnaghan material, Eq. (4.6). The principal wave effect consists of the propagation of a linear harmonic wave with the same amplitude and frequency as the harmonic excitation. This first harmonic is accompanied by a generated second harmonic wave with a spatially dependent amplitude as discussed by Cattani and Rutchisky [43]. Unlike the first harmonic response, the second harmonic generation is a direct sequel of the nonlinearity of the models, which is reflected by the additional dependency of its amplitude on Murnaghan's third order constants A, B, and C.

Of more interest, however, are the last two expressions of Eq. (4.28), which represent the transverse response of the formulated model to longitudinal harmonic excitation. In comparing to Eq. (4.11), it is observed that unlike Murnaghan

materials of Eq. (4.6), the formulated material manifests a transverse response to purely longitudinal harmonic excitation at the boundary. The response, as observed in Eq. (4.28), is a spatially modulated composite wave propagating with double the excitation frequency and an amplitude dependent on the introduced third order coupling constant α. The transverse response of the formulated material of Eq. (4.13) is uncharacteristic of any known material including Murnaghan materials. Through this analysis, there is evidence that a transfer of energy from longitudinal to transverse wave propagation modes is theoretically achievable through a mere modification to the Murnaghan strain energy function with the addition a single third order material constant as shown in Eq. (4.13).

4.3.3 Response to transverse harmonic excitation at the boundary

Although the response to longitudinal harmonic excitation is of more relevance to the problem of interest, the response of Eq. (4.13) to purely transverse harmonic excitation was also explored using the Straightforward Expansion. This necessitates solving Eq. (4.15) with the set of initial and boundary conditions of Eq. (4.29). Here, only horizontally polarized transverse wave (SH wave) is prescribed at the boundary of the semi-infinite half space.

$$\begin{aligned}
&u_1(x_1,0) = u_{1,t}(x_1,0) = 0,\ 0 \le x_1 < \infty \qquad u_1(0,t) = 0,\ t > 0 \\
&u_2(x_1,0) = u_{2,t}(x_1,0) = 0,\ 0 \le x_1 < \infty \qquad u_2(0,t) = U_2 cos(\omega t),\ t > 0 \\
&u_3(x_1,0) = u_{3,t}(x_1,0) = 0,\ 0 \le x_1 < \infty \qquad u_3(0,t) = 0,\ t > 0
\end{aligned} \tag{4.29}$$

Proceeding as before, the boundary conditions can be rewritten as given in Eq.4.30 below.

$$\begin{aligned} u_1(0,t) &= 0 \text{ for } t > 0 \\ u_2(0,t) &= \epsilon U_2 cos(\omega t) 0 \\ u_2(0,t) &= 0 \end{aligned} \tag{4.30}$$

Here, U_2 is the amplitude of the transverse harmonic excitation. This leads to the following expansion boundary conditions Eq. (4.31) for the perturbation analysis.

$$\begin{aligned} u_1^{(n)}(x_1,0) &= 0 \qquad & u_1^{(n)}(0,t) &= 0 \\ u_2^{(1)}(x_1,0) &= 0 \qquad & u_2^{(1)}(0,t) &= U_2 cos(\omega t) \\ & & u_2^{(n)}(0,t) &= 0 \\ u_3^{(n)}(x_1,0) &= 0 \qquad & u_3^{(n)}(0,t) &= 0 \end{aligned} \tag{4.31}$$

On substituting the assumed perturbation solution of Eq. (4.18) into Eq. (4.15), and collecting terms of various exponents of ϵ as before results in the following equations and associated solutions:

Order (ϵ):

$$\begin{aligned} u_{1,tt}^{(1)} - c_1^2 u_{1,11}^{(1)} &= 0, \text{ with } u_1^{(1)}(0,t) = 0 \\ u_{2,tt}^{(1)} - c_2^2 u_{2,11}^{(1)} &= 0, \text{ with } u_2^{(1)}(0,t) = U_2 cos(\omega t) \\ u_{3,tt}^{(1)} - c_3^2 u_{3,11}^{(1)} &= 0, \text{ with } u_3^{(1)}(0,t) = 0 \end{aligned} \tag{4.32}$$

$u_1^{(1)}(x_1,t) = 0,\ u_2^{(1)}(x_1,t) = U_2 \cos(k_2 x_1 - \omega t),\ u_3^{(1)}(x_1,t) = 0$

Order (ϵ^2):

$$\begin{aligned} u^{(2)}_{1,tt} - c_1^2 u^{(2)}_{1,11} &= \frac{N_2}{\rho} u^{(1)}_{2,1} u^{(1)}_{2,11}, \text{ with } u^{(2)}_1(0,t) = 0 \\ u^{(2)}_{2,tt} - c_2^2 u^{(2)}_{2,11} &= 0, \text{ with } u^{(2)}_2(0,t) = 0 \\ u^{(2)}_{3,tt} - c_3^2 u^{(2)}_{3,11} &= 0, \text{ with } u^{(2)}_3(0,t) = 0 \end{aligned} \tag{4.33}$$

On substituting in the above equations, the obtained solutions at order ϵ lead to:

Order (ϵ^2):

$$\begin{aligned} u^{(2)}_{1,tt} - c_1^2 u^{(2)}_{1,11} &= \frac{N_3}{2\rho} U_2^2 k_2^3 \cos[2(k_1 x_1 - \omega t)], \text{ with } u^{(2)}_1(0,t) = 0 \\ u^{(2)}_{2,tt} - c_2^2 u^{(2)}_{2,11} &= 0, \text{ with } u^{(2)}_2(0,t) = 0 \\ u^{(2)}_{3,tt} - c_3^2 u^{(2)}_{3,11} &= 0, \text{ with } u^{(2)}_3(0,t) = 0 \end{aligned} \tag{4.34}$$

As a result, the solutions to Eq. (4.34) are found to be:

$$\begin{aligned} u^{(2)}_1(x_1,t) &= \frac{N_3}{4\rho(c_1^2 - c_2^2)} U_2^2 k_2 \sin[(k_2 - k_1)x_1] \cos[(k_1 + k_2)x_1 - 2\omega t)] \\ u^{(2)}_2(x_1,t) &= 0 \\ u^{(2)}_3(x_1,t) &= 0 \end{aligned} \tag{4.35}$$

Stopping at order ϵ^2 as before, the Straightforward Expansion solution can be constructed from Eq. (4.18) and is shown below in Eq. (4.36).

$$\begin{aligned} u_1(x_1,t,\epsilon) &= \epsilon^2 \frac{N_3}{4\rho(c_1^2 - c_2^2)} U_2^2 k_2 \sin[(k_2 - k_1)x_1] \cos[(k_1 + k_2)x_1 - 2\omega t)] \\ u_2(x_1,t,\epsilon) &= \epsilon U_2 \cos(k_2 x_1 - \omega t) \\ u_3(x_1,t,\epsilon) &= 0 \end{aligned} \tag{4.36}$$

The solution to transverse harmonic excitation at the boundary, Eq. (4.36), is as expected. A longitudinal response is observed from a purely transverse harmonic excitation due to the inherent coupling in the formulated material model of Eq. (4.13) similar to that of Murnaghan material of Eq. (4.6), which was demonstrated by Cattani and Rushchitsky [43] by using the Successive Approximations method.

4.4 Summary

An analytical investigation is presented for the formulation of a hyper-elastic material in which one exploits nonlinear couplings and nonlinear wave phenomena to transfer energy from longitudinal to transverse wave propagation mode during plane wave propagation. Starting from the classical Murnaghan strain energy function, it was shown that through the introduction of an additional third order material parameter, which serves as a coupling term, a hyper-elastic material can be formulated that achieves the sought energy transfer. The response of the formulated material for small but finite longitudinal and transverse harmonic excitation at the boundary was explored using the straightforward expansion. Through the solution of perturbation analysis, it is shown that, unlike any existing materials including Murnaghan material, the formulated material manifests a transverse response to a purely longitudinal disturbance. Such material, if physically realizable through metamaterial technology, would be more amenable to controlling acoustic wave propagation path than conventional solids, in which competing longitudinal and transverse wave energy transport mechanisms complicate the refractive behavior.

Chapter 5: Summary, Conclusions, and Recommendations for Future Work

In the present chapter, the author provides concluding remarks and makes recommendations for future work. The overall goal of this dissertation work was to explore wave redirection mechanisms that takes advantage of materials with peculiar properties such as metamaterials and nonlinear transformation based approaches. The specific objectives included the following: a) examine various approaches, including the use of geometric transformations and b) explore modifications to constitutive laws to formulate material that can be use for the redirection of waves for practical applications. To address these objectives, the following was carried out: i) determination of a sequence of nonlinear transformations that can be used to formulate cloaking devices (electromagnetic and acoustic) for two- dimensional airfoil geometries by using the classical transformation method of wave redirection. ii) exploitation of nonlinearities and nonlinear phenomena to formulate a hyper-elastic material that can be useful for the redirection of acoustic waves. The contributions of this work are expected to be of benefit to metamaterials research and wave redirection, and in the area of nonlinear phenomena and their applications.

5.1 Summary and Conclusions

The authors effort to achieve the first objective of the investigation resulted in a sequence of transformations that can be used to map a symmetric Karman-Trefftz airfoil disk bounded by two circular arcs, to a symmetric Karman-Trefftz airfoil annulus whilst keeping the outer boundary unchanged. Based on the premises of the transformation approach to cloaking, the found sequence of transformations can be used to formulate airfoil cloaking devices for both electromagnetic and acoustic fields. To do so, it is required to determine the deformation gradient of the composite of the found transformations, a task that may necessitate the use of a numerical tool as the found sequence could not be combined to one explicit mapping of Cartesian or polar coordinate variables. An initial effort using the Joukowski transformation, a special case of the Karman-Trefftz transformation, was only partially successful. If the remaining transformation in the aforementioned approach based on the relatively simpler Joukowski transformation is determined in the future, it could lead to a sequence of transformations for which an explicit composite map would transpire, and the required displacement gradient could be determined analytically. Nonetheless, the found solution based on the properties of the Karman-Trefftz transformation, despite its relative complexity, is expected to be useful for formulating cloaks for practical airfoils. In contrast to Joukowski transformation that leads to non-realistic airfoils with a cusp at the trailing edge, the Karman-Trefftz transformation leads to airfoils with finite trailing edge angles. Furthermore, the Karman-Trefftz transformation presents means to control the characteristics of

the airfoil that are attractive to approximating practical airfoils such as NACA series of airfoils.

To achieve the second objective of the investigation, the author took advantage of nonlinear wave phenomena to formulate a hyper-elastic material that manifests a transverse response to a longitudinal plane wave perturbation at its boundary. Specifically, the author exploited nonlinear couplings opportunities available in the third order Murnaghan strain energy function, to couple wave propagation modes in a way that is favorable to a transfer of energy from longitudinal mode to transverse mode. By using approximation and perturbation techniques, the formulated material was investigated for the propagation of plane longitudinal and transverse waves at the boundary of an infinite half space. It was shown that a purely longitudinal plane wave excitation at the boundary resulted in both a longitudinal response and a transverse response of the formulated material. Such a response is uncharacteristic to any known material, including Murnaghan materials, and can be useful for the redirection of acoustic waves. The redirection of acoustic waves by using the refractive properties of solid elastic materials is challenging because of the inherent presence of transverse wave, which refracts differently than their faster longitudinal counterparts. This remains an active area of research.

5.2 Recommendations for future work

The present investigation led to a sequence of transformations that is only applicable to symmetric Karman-Trefftz airfoils bounded by two circular segments.

It would be interesting to explore means that can be use to extend the finding to more general Karman-Trefftz airfoils, including cambered airfoils. The overall objective is to formulate cloaking devices for practical airfoils, for example NACA family of airfoils, which can be well approximated by using general Karman-Trefftz airfoils.

Also, although the geometric outcome of combining the found transformations is consistent with the premises of the transformation approach to cloaking, numerical simulations should be conducted to assess the performance of a transformation based airfoil cloak formulated by using the found transformations. This is particularly important as the combination of the transformations in the sequence appears to result in both radial and angular changes of the initial coordinates of mapped points. These effects of the angular changes, if any, would be interesting to observe numerically and may need to be addressed if perfect cloaking is sought theoretically. Numerical simulations can present challenging, however, without an explicit formulation of the deformation gradient. Furthermore, it is likely that discrete material properties would be needed for the numerical simulations, which may required interpolation of tensor like quantities; a task that is not trivial and need to be approached with caution. This is because the transformation approach leads to tensor like quantities for the material properties; that is, the permitivity and permeability for electromagnetics, and the density and bulk modulus for acoustics.

It would also be interesting to find the final transformation needed to complete the sought-after transformations sequence based on the Joukowski transformation. This can lead to a less daunting task to formulate the parameters of an airfoil cloak

using the transformation equations. Consequently, the simulation effort to assess the performance of the formulated cloak could be significantly less challenging.

The formulated hyper-elastic material can be assessed numerically to validate the postulated hypothesis, and the results found in the analysis. The model has been challenging to implement in the numerical finite element tool Comsol because of the formulation based on the displacement gradients instead of the components of the deformation gradient tensor. However, it may be possible to reformulate the formulation in term of the deformation gradient tensor instead of the displacement gradient tensor by using equations of continuum mechanics that relate the two measures of deformation. It is also likely that the numerical simulation would be feasible by using future versions of Comsol multiphysics as suggested by the software development team of the company.

Finally, it is an entire area of investigation to determine means to practically achieve the nonlinear couplings in the manner that was analytically achieved in the constitutive law as of the formulated material. One avenue may be to look into inclusions in a polymer-based material and metamaterials technology.

Bibliography

[1] D.M. Hernndez. *Fundamentals and Basic Optical Instruments*. Optical Science and Engineering. CRC Press, 2017.

[2] R.J. Urick. *Principles of Underwater Sound*. Peninsula Publishing, 1983.

[3] B. Banerjee. *An Introduction to Metamaterials and Waves in Composites*. Taylor & Francis, 2011.

[4] V. G. Veselago. The electrodynamics of substances with simultaneously negative values of ε and μ. *Soviet Physics Uspekhi*, 10(4):509, April 1968.

[5] R.V. Craster and S. Guenneau. *Acoustic Metamaterials: Negative Refraction, Imaging, Lensing and Cloaking*. Springer Series in Materials Science. Springer, 2012.

[6] R. A. Shelby, D. R. Smith, and S. Schultz. Experimental verification of a negative index of refraction. *Science*, 292(5514):77–79, 2001.

[7] J. B. Pendry and S. A. Ramakrishna. Focusing light using negative refraction. *Journal of Physics: Condensed Matter*, 15(37):6345, September 2003.

[8] J. B. Pendry, D. Schurig, and D. R. Smith. Controlling Electromagnetic Fields. *Science*, 312(5781):1780–1782, June 2006.

[9] D. Schurig, J. J. Mock, B. J. Justice, S. A. Cummer, J. B. Pendry, A. F. Starr, and D. R. Smith. Metamaterial Electromagnetic Cloak at Microwave Frequencies. *Science*, 314(5801):977–980, November 2006.

[10] G. W. Milton, M. Briane, and J. R. Willis. On cloaking for elasticity and physical equations with a transformation invariant form. *New Journal of Physics*, 8(10):248, October 2006.

[11] G.A. Holzapfel. *Nonlinear Solid Mechanics: A Continuum Approach for Engineering*. Wiley, 2000.

[12] A. Lichnerowicz, J.W. Leech, and D.J. Newman. *Elements of Tensor Calculus*. Dover Books on Mathematics. Dover Publications, 2016.

[13] S. A. Cummer and D. Schurig. One path to acoustic cloaking. *New Journal of Physics*, 9(3):45, March 2007.

[14] H. Chen and C. T. Chan. Acoustic cloaking and transformation acoustics. *Journal of Physics D: Applied Physics*, 43(11):113001, March 2010.

[15] M. Rahm, D. Schurig, D. A. Roberts, S. A. Cummer, D. R. Smith, and J. B. Pendry. Design of electromagnetic cloaks and concentrators using form-invariant coordinate transformations of Maxwells equations. *Photonics and Nanostructures - Fundamentals and Applications*, 6(1):87–95, April 2008.

[16] Z. J. Wong, Y. Wang, K. OBrien, J. Rho, X. Yin, S. Zhang, N. Fang, T. Yen, and X. Zhang. Optical and acoustic metamaterials: superlens, negative refractive index and invisibility cloak. *Journal of Optics*, 19(8):084007, August 2017.

[17] I. H. Abbott. *Theory of Wing Sections, Including a Summary of Airfoil Data*. Courier Dover Publications, 1959.

[18] I. H. Abbott, E. V. Albert, and S. S. Louis. Summary of airfoil data. Technical report, DTIC Document, 1945.

[19] R. S. Burington. On the Use of Conformal Mapping in Shaping Wing Profiles. *The American Mathematical Monthly*, 47(6):362, June 1940.

[20] N. R. Kapania, K. Terracciano, and S. Taylor. *Modeling the Fluid Flow around Airfoils Using Conformal Mapping*. 2008.

[21] R. Schinzinger and P.A.A. Laura. *Conformal Mapping: Methods and Applications*. Dover Books on Mathematics Series. Dover Publications, 2003.

[22] G. A. Chaney. *The application of conformal representations to the Fuchsian differential equation ofsecond order and the Schwarzian differential equation of the third order*. University of Wisconsin–Madison, 1911.

[23] G. F. Carrier, M. Krook, and C. E. Pearson. *Functions of a Complex Variable: Theory and Technique*. Hod Books, January 1983.

[24] J. J. H Blom. Some characteric quatities of karman-trefftz profiles. Technical report, DTIC Document, 1983.

[25] R.V. Churchill and J.W. Brown. *Complex Variables and Applications*. International student edition. McGraw-Hill, 1984.

[26] H. Kober. *Dictionary of Conformal Representation*. Dover Publications, 1957.

[27] Rami Shakarchi. *Inverse Mapping Theorem*, pages 303–326. Springer New York, New York, NY, 1998.

[28] Serge Lang. The Riemann Mapping Theorem. In Serge Lang, editor, *Complex Analysis*, pages 306–321. Springer New York, New York, NY, 1999.

[29] L.L. Pennisi. *Elements of Complex Variables*. Holt, Rinehart and Winston, 1974.

[30] A. Bedford and D.S. Drumheller. *Introduction to Elastic Wave Propagation*. Wiley, 1996.

[31] A. N. Norris. Acoustic cloaking theory. *Proceedings of the Royal Society A: Mathematical, Physical and Engineering Science*, 464(2097):2411–2434, September 2008.

[32] G. W. Milton and A. V. Cherkaev. Which Elasticity Tensors are Realizable? *Journal of Engineering Materials and Technology*, 117(4):483–493, October 1995.

[33] M. Kadic, T. Buckmann, N. Stenger, M. Thiel, and M. Wegener. On the practicability of pentamode mechanical metamaterials. *Applied Physics Letters*, 100(19):191901, 2012.

[34] D.S. Drumheller. *Introduction to Wave Propagation in Nonlinear Fluids and Solids*. Cambridge University Press, 1998.

[35] A. J. Dick, B. Balachandran, and C. D. Mote Jr. Intrinsic localized modes in microresonator arrays and their relationship to nonlinear vibration modes. *Nonlinear Dynamics*, 54(1-2):13–29, October 2008.

[36] F. D. Murnaghan. Finite Deformations of an Elastic Solid. *American Journal of Mathematics*, 59(2):235, April 1937.

[37] J. J. Rushchitsky. *Nonlinear Elastic Waves in Materials*. Foundations of Engineering Mechanics. Springer International Publishing, Cham, 2014.

[38] C. Cattani and J. J. Rushchitsky. Cubically nonlinear versus quadratically nonlinear elastic waves: Main wave effects. *International Applied Mechanics*, 39(12):1361–1399, 2003.

[39] J. J. Rushchitsky. On the Constants of the Nonlinear Murnaghans Hyperelastic Material Model. *International Applied Mechanics*, 52(5):508–519, September 2016.

[40] A. Wazwaz. *Partial Differential Equations and Solitary Waves Theory*. Springer-Verlag Berlin Heidelberg, Berlin, Heidelberg, 2009. OCLC: 654362074.

[41] A.H. Nayfeh. *Introduction to Perturbation Techniques*. Wiley, 2011.

[42] A. Kirsch. *An Introduction to the Mathematical Theory of Inverse Problems*, volume 120 of *Applied Mathematical Sciences*. Springer New York, New York, NY, 2011.

[43] C. Cattani and J. J. Rushchitsky. Cubically nonlinear elastic waves: wave equations and methods of analysis. *International applied mechanics*, 39(10):1115–1145, 2003.